Modeling and ID Compensation of TRIBs Beam Optics at the MAX IV 1.5 GeV Storage Ring

Alfred Petersson

Supervisors:
Francis Cullinan* and David K Olsson*

February 2026

Abstract

Transverse Resonant Island Buckets (TRIBs) is a promising method for pseudo-single bunch delivery in the MAX IV 1.5 GeV storage ring. In this thesis, a theoretical model of the non-linear optics based on resonant Hamiltonian mechanics is applied to the TRIBs optics. Measurement techniques for characterizing the TRIBs orbit are developed and tested and compared with theoretical predictions and numerical tracking. As the TRIBs optics in the 1.5 GeV ring has previously been found to be sensitive to the impact of insertion devices (IDs), the effects of the IDs are analyzed in the Hamiltonian framework. A novel sextupole correction scheme for TRIBs optics ID compensation is presented, achieved by optimizing the sextupole magnet strengths such that the parameters of the resonant Hamiltonian stay constant. A potential feedforward implementation of the compensation scheme is tested, which is successfully used to correct for an ID.

*MAX IV

Contents

1 Introduction **4**

2 Linear Optics and Longitudinal Dynamics **7**
- 2.1 The Frenet-Serret Coordinate System 7
- 2.2 The Multipole Expansion 7
- 2.3 Transverse Linear Optics 8
  - 2.3.1 Betatron Motion 8
  - 2.3.2 Normalized Phase Space and Action-Angle Variables . . . 11
  - 2.3.3 Resonances 12
- 2.4 Longitudinal Dynamics 13
- 2.5 Dispersion and Chromaticity 14
- 2.6 Hamiltonian Mechanics 15

3 Non-linear Optics **17**
- 3.1 The Non-resonant Hamiltonian 17
  - 3.1.1 First-order Perturbation Theory 18
  - 3.1.2 Second-order Perturbation Theory 19
- 3.2 The Resonant Hamiltonian 20
  - 3.2.1 The TRIBs Parameters 22
  - 3.2.2 Stable Fixed Points of the Hamiltonian 23
  - 3.2.3 The Island Tunes 23
  - 3.2.4 Efficient Numerical Computation of TRIBs Parameters . 25

4 The MAX IV 1.5 GeV Storage Ring **28**
- 4.1 Insertion Devices 29
- 4.2 Lattice Modeling in Accelerator Toolbox 29
  - 4.2.1 LOCO Measurements 30
  - 4.2.2 Modeling of Insertion Devices 31
  - 4.2.3 Tune Adjustment 32

5 Measurements of TRIBs Orbits at MAX IV **33**
- 5.1 Imaging Using Diagnostic Beamlines 34
  - 5.1.1 Reconstruction of Island Orbits 34
- 5.2 Experimental Measurement of TRIBs Parameters 37
  - 5.2.1 The Tune Scan Technique 37
  - 5.2.2 The Island Tune Technique 39
  - 5.2.3 Measuring the Island Orbit Phase Advance 39
  - 5.2.4 Evaluation of TRIBs Parameter Measurements 40
  - 5.2.5 Online Readback of the TRIBs Parameters 43
- 5.3 Limitations of the Analytical Hamiltonian 44
- 5.4 Single Island Measurements 45
  - 5.4.1 Measurement and Optimization of Island Populations . . 46
  - 5.4.2 Correcting for Island Populations 47
  - 5.4.3 Turn-by-turn BPM Measurements 48

5.4.4 Bunch-by-Bunch Measurements 49

6 Compensation of Insertion Devices 52

6.1 Correcting the TRIBs Parameters 52

6.2 Measurements of the TRIBs ID Compensation 54

6.2.1 Measured Versus Theoretical TRIBs Parameters 56

6.2.2 Lifetime 58

6.3 Future Implementation 59

7 Conclusions and Outlook 61

Appendices 67

A Detailed Second-order Calculations 67

B Calibration of Optical Magnification 69

C Detailed Tune Scan Implementation 71

1 Introduction

Particle accelerators have a wide array of uses ranging from fundamental science to industry. *Synchrotron light sources* are a subset of particle accelerators that utilize the strong *synchrotron radiation* (SR) emitted as a beam, typically of electrons, is bent by magnetic fields. In a synchrotron *storage ring*, the particle beam is bent into a closed loop and, in third- and fourth-generation storage rings, the SR used is mostly produced by specialized *insertion devices* (IDs). Depending on beam and ID properties, these IDs can produce high brightness and well focused electromagnetic radiation, typically in the UV to hard X-ray regime. The synchrotron radiation produced by an ID (or in some cases, a bending magnet) is directed to a *beamline*, where it can be used for applications in life sciences, biomedical research, nanoscience and nanotechnology, industrial research, and more [1].

MAX IV is a light-source facility in Lund, Sweden. The facility houses a third generation 1.5 GeV storage ring, a fourth generation 3 GeV storage ring and the Short Pulse Facility driven by a linear accelerator, which also provides continuous top-up injection of both storage rings. The 1.5 GeV storage ring, which will be the focus of this thesis, is optimized for the production of soft X-ray and UV radiation [2].

As a consequence of the the oscillating electric fields that are used to accelerate the stored beam in a synchrotron, the beam is not continuous along the length of the ring, but consists of separate *bunches*. The electromagnetic potential wells containing the bunches are called *RF buckets*. Both storage rings at MAX IV are usually operated in *multi-bunch* mode, where the RF buckets are populated as evenly as practical. This generally allows for the storage of as much beam current as possible, in turn maximizing the amount of SR produced.

Certain measurement techniques used by the beamlines at the 1.5 GeV ring require greater separation in time between each of the SR pulses. This can be achieved by *single-bunch* operation, where only one of the RF buckets is populated with electrons. However, reducing the number of bunches decreases the total amount of SR produced, often to the detriment of other beamlines. As a result, MAX IV currently only schedules two full weeks of single-bunch operation per year.

One proposed way to alleviate this trade-off between single- and multi-bunch operation is the use of *Transverse Resonance Island Buckets* (TRIBs). By carefully exciting a third-order transverse resonance, it is possible to create a secondary stable orbit that oscillates transversely around the usual core orbit, closing after three turns around the machine. It is then possible to populate this *island orbit* in only one of the RF buckets. The horizontal offset between the two orbits allows each of the beamlines to selectively observe the SR from either the island

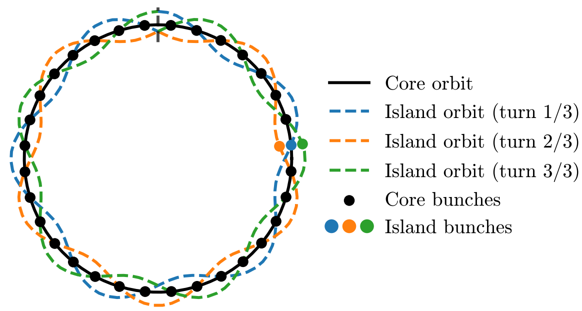

Figure 1.1: Conceptual illustration showing the island orbit compared to the core orbit. The diagram is not to scale.

or core orbit, effectively choosing between single- or multi-bunch operation in what is called pseudo single-bunch delivery [3–5].

TRIBs have been experimentally demonstrated in both storage rings at MAX IV. Initial user tests were conducted in 2021 on the 1.5 GeV ring where the beamlines FlexPES and FinEstBeAMS, the two beamlines regularly utilizing single-bunch techniques, were able to successfully utilize the SR from the TRIBs orbit [3]. These initial tests demonstrated the feasibility of TRIBs as a way of achieving pseudo single-bunch delivery in the 1.5 GeV ring. The wavelength of SR from each ID can be tuned by adjusting the gap between the magnets in the ID, and one of the main challenges identified was that the TRIBs optics was found to be very sensitive to these ID gap changes. TRIBs has since been developed into a deliverable operation mode, and in November 2024 a user test week was dedicated to testing the TRIBs mode of the 1.5 GeV ring both operationally and from the perspective of the users [6]. To mitigate the impact of ID gap movements, restrictions were put in place on some of the ID gaps, thus limiting the wavelengths available to those beamlines. Additionally, the beamlines were not allowed to move the ID gap during top-up injections. The feedback from the user beamlines indicated that both restrictions would have a major impact on the operation of some of the beamlines.

The goal of this thesis is to further the understanding of the TRIBs optics in the 1.5 GeV ring and in turn develop possible solutions for compensating the impact of varying ID gaps. The TRIBs are mainly described within the framework of non-linear Hamiltonian dynamics, wherein a relatively simple resonant Hamiltonian can be used to describe the island buckets in phase space [4, 5]. Different measurement techniques for the characterization of the TRIBs orbits are developed and evaluated. A novel, targeted scheme for ID compensation of the TRIBs optics is derived. By adjusting the sextupole magnets without affecting the linear optics, the non-linear dynamics, as described by a resonant

Hamiltonian, is kept constant for varying ID gaps. This compensation scheme is evaluated using the aforementioned measurement techniques and compared with both analytical calculations and simulation via tracking. The future practical implementation of this correction scheme is discussed, such as the development of a feedforward or feedback device for ID compensation.

2 Linear Optics and Longitudinal Dynamics

The field of accelerator physics is expansive. This section is intended to summarize only the most relevant theory needed for later sections, in addition to clarifying the definitions, conventions and notations used.

2.1 The Frenet-Serret Coordinate System

The coordinate system of choice in accelerator physics is the *Frenet-Serret coordinate system*. This curvilinear coordinate system describes the positions of the particles in relation to an idealized *reference particle* following the *reference orbit*. Any point along this orbit can be specified by the longitudinal coordinate s, given by the path length from a fixed origin $s = 0$. In a storage ring (as opposed to a linear accelerator), the reference orbit forms a closed loop with total circumference C such that s and $s + C$ both refer to the same position along the ring. The relativistic momentum of the reference particle is by definition the *reference momentum* p_0.

Let the position of the reference particle be $\mathbf{r_0}(s)$. In the Frenet-Serret coordinate system, the position $\mathbf{r}(s)$ of any particle is specified in relation to the reference particle according to [7]

$$\mathbf{r}(s) = \mathbf{r_0}(s) + x\hat{\mathbf{x}}(s) + y\hat{\mathbf{y}}(s) + z\hat{\mathbf{z}}(s), \tag{2.1}$$

as shown in Fig 2.1. The longitudinal basis vector $\hat{\mathbf{z}}(s) = \frac{\partial \mathbf{r_0}}{\partial s}$ is parallel to the reference orbit at s while the horizontal basis vector $\hat{\mathbf{x}}(s) = -\rho(s)\frac{\partial \hat{\mathbf{z}}}{\partial s}$ points outward away from the ring center (normalized using the radius of curvature $\rho(s)$ of the reference orbit). The vertical basis vector is then defined to be $\hat{\mathbf{y}}(s) = -\hat{\mathbf{z}}(s) \times \hat{\mathbf{x}}(s)$ so as to form a right-handed orthonormal basis for each s along the ring [7].

2.2 The Multipole Expansion

The particles in any accelerator are almost exclusively manipulated using transverse magnetic fields. To describe an arbitrary transverse magnetic field $\mathbf{B} = B_x(x, y)\hat{\mathbf{x}} + B_y(x, y)\hat{\mathbf{y}}$, we introduce the multipole expansion [7]

$$B_y(x, y) + iB_x(x, y) = \sum_{n=0}^{\infty}(b_n + ia_n)(x + iy)^n. \tag{2.2}$$

The first few magnetic field components are called *dipole*, *quadrupole*, *sextupole* and *octupole* fields, from $n = 0$ to $n = 3$ respectively. By convention, magnetic fields corresponding to the terms b_n are called *normal* fields, while *skew* fields correspond to the terms a_n. The first few normal field components are illustrated in Fig. 2.2. Normalized to the reference momentum p_0 and particle change

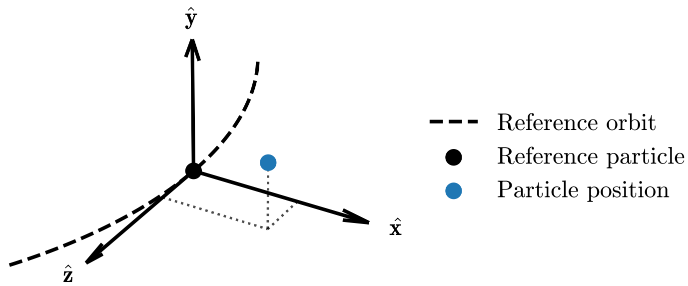

Figure 2.1: An illustration of the Frenet-Serret coordinate system showing the reference particle, the basis vectors $\hat{\mathbf{x}}$, $\hat{\mathbf{y}}$, and $\hat{\mathbf{z}}$, and an example of an arbitrary particle position.

q, the normal and skew multipole strengths k_n and j_n in Eq. (2.2) are given by [4]

$$\begin{aligned} k_n &= \frac{q}{p_0} \left. \frac{\partial^n B_y}{\partial x^n} \right|_{x=y=0} = \frac{q}{p_0} n!\, b_n, \\ j_n &= \frac{q}{p_0} \left. \frac{\partial^n B_x}{\partial y^n} \right|_{x=y=0} = \frac{q}{p_0} n!\, a_n. \end{aligned} \tag{2.3}$$

2.3 Transverse Linear Optics

Linear optics, as the name suggests, only considers the fields which vary linearly with respect to x and y, namely dipole and quadrupole fields. If only the linear transverse effects are considered, the equations of motion have relatively simple closed-form solutions which makes it an extremely useful tool. For now, we therefore disregard the effects of higher-order multipoles and longitudinal effects. In addition, the horizontal and vertical planes will mostly be considered separately for simplicity.

2.3.1 Betatron Motion

Normal dipoles are used to bend the orbit horizontally around the ring. The bending radius ρ of a beam of particles with the longitudinal relativistic momentum p_z and charge q is given by

$$B_y \rho = \frac{p_z}{q}. \tag{2.4}$$

Comparing with Eqs. (2.2) and (2.3), note that $B_y = b_0$ and $k_0 = 1/\rho$ for an on-momentum particle with $p_z = p_0$.

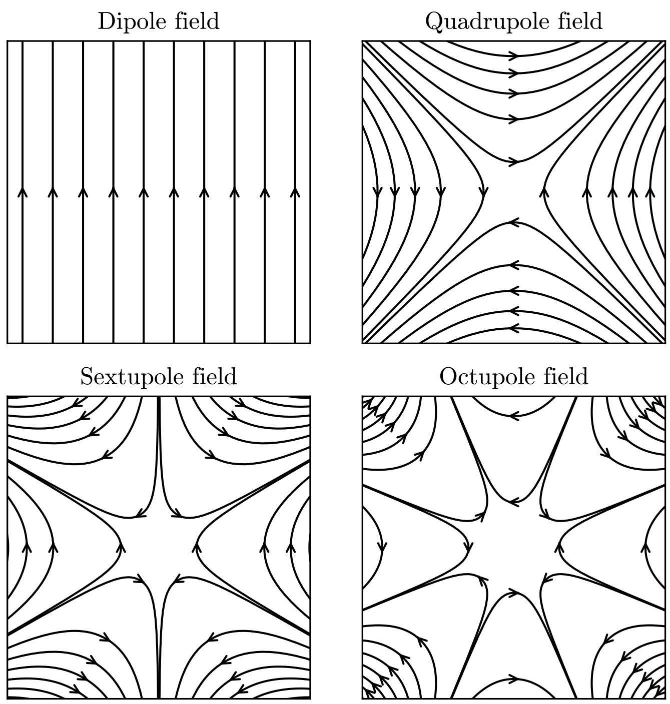

Figure 2.2: An illustration of the first few normal multipole components, where the density of field lines is proportional to the relative magnetic field strength.

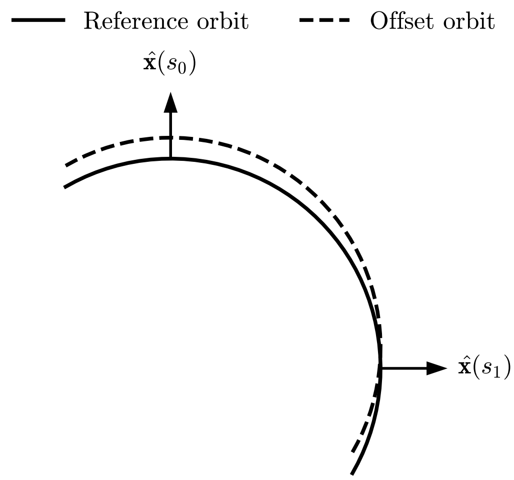

Figure 2.3: A diagram illustrating the principle of weak focusing. A particle with an offset purely in x at s_0 will cross the reference orbit at some point s_1, even if the bending radius is identical.

The motion of the particles around the storage ring would not be stable without some kind of restoring force, which allows particles that deviate from the reference orbit to be driven back toward it. In the case of synchrotrons, there are two main contributors to such a force: weak and strong focusing. Strong focusing is achieved using quadrupole magnets, whose field strength varies linearly with x and y. For a normal quadrupole, the field is given by

$$\begin{aligned} B_x(x, y) &= gy, \\ B_y(x, y) &= -gx, \end{aligned} \tag{2.5}$$

where $g = b_1 = \frac{p_0}{q} k_1$ is the field gradient. The varying field results in particles being focused along one axis, while the difference in sign means that the quadrupole must have a de-focusing effect along the other axis. This fundamental limitation of quadrupole magnets is overcome by alternating between focusing and de-focusing magnets, which can be arranged to achieve a net focusing effect.

By contrast, weak focusing is a geometric effect of the bending dipoles. It can intuitively be understood by considering two particles entering a dipole parallel to each other with a small offset in x. The paths of the two particles will start to converge since any two similar circles offset by less than their diameter will cross, as illustrated in Fig. 2.3. The strong- and weak focusing result in the second-order ordinary differential equations [7]

$$\begin{aligned} x'' + K_x(s)x &= 0, \\ y'' + K_y(s)y &= 0. \end{aligned} \tag{2.6}$$

where $K_x(s) = k_1(s) + 1/\rho^2(s)$ and $K_y(s) = -k_1(s)$. The term $1/\rho^2(s)$ arises due to weak focusing.

Let u be a placeholder for x or y. Equation (2.6) is a so-called pseudo-harmonic oscillator which has the solutions [8]

$$u(s) = a_0\sqrt{\beta_u(s)}\cos\left(\mu_u(s) + b_0\right), \tag{2.7}$$

where a_0 and b_0 depend on the initial conditions for each particle. This oscillating motion is called *betatron motion* or *betatron oscillation*. The functions $\beta_u(s)$ and $\mu_u(s)$, often called the *beta function* and *phase advance* respectively, are fundamental quantities in linear optics. For a storage ring, the beta function is uniquely defined and given by [7]

$$\begin{gathered}\frac{1}{2}\beta_u(s) + K_u(s)\beta_u(s) - \frac{1}{\beta_u(s)}\left[1 + \left(\frac{\beta_u'(s)}{2}\right)\right] = 0,\\ \beta_u(0) = \beta_u(C), \quad \beta_u'(0) = \beta_u'(C).\end{gathered} \tag{2.8}$$

where the periodic boundary conditions guarantee that β_u is continuous and differentiable over the ring. The phase advance is given by

$$\mu_u(s) = \int_0^s \mathrm{d}s'\,\frac{1}{\beta_u(s')}. \tag{2.9}$$

The beta function β_u is one of the three *Courant-Snyder parameters* (CS parameters), the remaining two of which are given by [7]

$$\begin{aligned}\alpha_u(s) &= -\frac{\beta_u'(s)}{2},\\ \gamma_u(s) &= \frac{1 + \alpha_u^2(s)}{\beta_u(s)}.\end{aligned} \tag{2.10}$$

The CS parameters, together with the phase advance, conveniently describes the linear betatron motion of a particle in *phase space*. Since both the position and velocity is required to describe the state of a particle in an accelerator, the (transverse) phase space coordinates of a particle can be given by x, x', y and y', where $u' = \frac{\mathrm{d}u}{\mathrm{d}s}$. Note that u' is small enough for any reasonable orbit that the small angle approximation is often used to express u' in units of angle.

2.3.2 Normalized Phase Space and Action-Angle Variables

The action of a linear lattice on a particle from the point s_0 to s_1 along the ring (ignoring longitudinal effects) is given by a linear transformation [7]

$$\begin{bmatrix} x \\ x' \\ y \\ y' \end{bmatrix}_{s_1} = \mathbf{M}_{s_0\to s_1}\begin{bmatrix} x \\ x' \\ y \\ y' \end{bmatrix}_{s_0}, \tag{2.11}$$

where the 4×4 matrix $\mathbf{M}_{s_0 \to s_1} = (m_{ij})$ is often referred to as the *transport matrix*. Now consider the case of uncoupled motion, where $\mathbf{M}_{s_0 \to s_1}$ is block diagonal such that the motion in each plane u is given by the 2×2 matrix $\mathbf{M}^{(u)}_{s_0 \to s_1} = (m^{(u)}_{ij})$

$$\begin{bmatrix} u \\ u' \end{bmatrix}_{s_1} = \mathbf{M}^{(u)}_{s_0 \to s_1} \begin{bmatrix} u \\ u' \end{bmatrix}_{s_0}. \tag{2.12}$$

It can be shown that this matrix can be factorized according to

$$\mathbf{M}^{(u)}_{s_0 \to s_1} = \begin{bmatrix} \sqrt{\beta_1} & 0 \\ -\alpha_1/\sqrt{\beta_1} & 1/\sqrt{\beta_1} \end{bmatrix} \begin{bmatrix} \cos\Delta\mu & \sin\Delta\mu \\ -\sin\Delta\mu & \cos\Delta\mu \end{bmatrix} \begin{bmatrix} 1/\sqrt{\beta_0} & 0 \\ \alpha_0/\sqrt{\beta_0} & \sqrt{\beta_0} \end{bmatrix}, \tag{2.13}$$

where $\beta_i = \beta_u(s_i)$ etc. and $\Delta\mu = \mu_1 - \mu_0$. By defining the *normalized coordinates* $\tilde{u}$ and $\tilde{u}'$ according to

$$\begin{bmatrix} \tilde{u} \\ \tilde{u}' \end{bmatrix} = \begin{bmatrix} 1/\sqrt{\beta} & 0 \\ \alpha/\sqrt{\beta} & \sqrt{\beta} \end{bmatrix} \begin{bmatrix} u \\ u' \end{bmatrix}, \tag{2.14}$$

it follows from Eqs. (2.13) and (2.14) that the linear transformation between s_0 and s_1 in *normalized phase space* is simply a rotation by the relative phase advance

$$\begin{bmatrix} \tilde{u} \\ \tilde{u}' \end{bmatrix}_{s_1} = \begin{bmatrix} \cos\Delta\mu & \sin\Delta\mu \\ -\sin\Delta\mu & \cos\Delta\mu \end{bmatrix} \begin{bmatrix} \tilde{u} \\ \tilde{u}' \end{bmatrix}_{s_0}. \tag{2.15}$$

Positions in normalized phase space are often specified using polar coordinates according to the *action-angle variables*

$$\begin{aligned} \tilde{u} &= \sqrt{2J_u}\cos\phi_u, \\ \tilde{u}' &= -\sqrt{2J_u}\sin\phi_u, \end{aligned} \tag{2.16}$$

where the action J_u denotes the amplitude and the angle ϕ_u the phase. The action-angle coordinate is a powerful tool which greatly simplifies the linear dynamics in the uncoupled case, as the transformation from s_0 and s_1 does not affect the action J_u while the angle simply increases with the phase advance

$$\begin{aligned} J_u^{(s_1)} &= J_u^{(s_0)}, \\ \phi_u^{(s_1)} &= \phi_u^{(s_0)} + \Delta\mu_u. \end{aligned} \tag{2.17}$$

2.3.3 Resonances

Over the course of a full revolution, the number of betatron oscillations is given by the tune

$$Q_u = \frac{\mu_u(C)}{2\pi}. \tag{2.18}$$

Now consider a particle that encounters a perturbation (such as small error in dipole strength) at a point s_0, resulting in a small kick $u' \to u' + \delta u'$. If Q_u is very near to an integer value I, the rotation matrix in Eq. (2.15) will be close to the identity matrix since $\Delta\mu_u \approx 2n\pi$. After one turn, the particle will therefore arrive at s_0 with the same phase space coordinates as the previous turn, and once again receive a kick such that $u' + \delta u' \rightarrow u' + 2\delta u'$. For each turn, the kicks accumulate in the same direction, and the particle will eventually be lost. If the tune was instead much further from integer, u' would oscillate between $u' > 0$ and $u' < 0$ such that the kicks $\delta u'$ tend to cancel out over many turns. This example motivates why the integer *resonance* $Q_u \approx n$ should in general be avoided.

Not only integer resonances should be avoided. Resonances can appear any time the resonance condition

$$n_x Q_x + n_y Q_y \approx I \tag{2.19}$$

is fulfilled for integers n_x, n_y, and I. How close the tune needs to be to each resonance for its effects to be noticeable is called the *stop band width*, and depends on various lattice properties [8]. Resonances are categorized into different orders, where an *n:th order resonance* is given by $|n_x| + |n_y| = n$. Lower order resonances are in general the most impactful, such as the first-order integer resonance discussed before. To induce TRIBs, the third-order resonance $3Q_x \approx I$ is exploited, as will be discussed in Section 3.2.

2.4 Longitudinal Dynamics

The particles in a ring are always losing momentum due to synchrotron radiation. This necessitates a mechanism for the particles to regain the lost energy, as they would otherwise start to spiral inwards due to the change in bending radius in the dipoles. In a synchrotron, this is done using *radio frequency cavities* (RF cavities), which are used to sustain an oscillating electric field mostly parallel to $\hat{\mathbf{z}}$. For a longitudinal electric field given by

$$E_z = E_0 \cos(2\pi f_{\mathrm{RF}} t), \tag{2.20}$$

the particles will experience a periodic force that will alternate between accelerating and decelerating the particles at the *RF frequency*, f_{RF}. In order for the cavity to provide a net energy increase, the RF frequency must be a multiple of the revolution frequency

$$f_{\mathrm{RF}} = h f_{\mathrm{rev}} \tag{2.21}$$

for a positive integer h called the *harmonic number*. This ensures that a particle that is accelerated during one turn arrives at roughly the same relative phase one turn later.

The RF frequency is selected to fulfill Eq. (2.21) for the revolution frequency of an on-momentum particle with $p_z = p_0$. Such a particle is called a *synchronous particle* when the energy gain from the RF cavity exactly matches the average energy loss per turn. Since the energy gain depends on the phase at which the particle reaches the RF cavity, a synchronous particle must arrive at the correct *synchronous phase*. Note that while there are two phases per RF cycle where the energy gain matches the energy loss, only one of these is stable [7].

We now define the longitudinal phase space variables δ and τ for a particle with longitudinal momentum p_z at a longitudinal distance z from the synchronous particle

$$\begin{aligned} \delta &= \frac{p_z - p_0}{p_0}, \\ \tau &= -\frac{z}{\beta_r c}, \end{aligned} \tag{2.22}$$

where β_r is the relativistic beta. Here, τ gives the relative arrival time compared to the synchronous particle. For a harmonic number h, there are h times during a revolution period where the phase of the RF cavity reaches the synchronous phase, meaning there are h stable regions in the longitudinal phase space evenly spaced around the storage ring called *RF buckets*. This means that the beam in a synchrotron cannot be continuous along the ring, but must be divided in (at most) h bunches of particles.

Inside each bucket, the particles in a bunch will not all be exactly synchronous. Because of this, the RF system is carefully designed so that particles with δ and τ small enough will oscillate in the longitudinal phase space. This results in both an *energy spread* and a *bunch length*.

2.5 Dispersion and Chromaticity

Due to the inevitable energy spread of the beam, the bending radius given in Eq. 2.4 will not be the same for all particles. This results in the stable orbit varying with the momentum deviation δ. To first order in energy, this shift in orbit is described using the *dispersion function* [7]

$$u_\delta(s) = \delta D_u(s) + \mathcal{O}(\delta^2), \tag{2.23}$$

where $\delta D_u(s)$ is given by

$$\begin{aligned} D_u''(s) + K_u(s) D_u(s) &= \frac{1}{\rho(s)}, \\ D_u(0) = D_u(C), \quad D_u'(0) &= D_u'(C). \end{aligned} \tag{2.24}$$

Note that in the ideal case without coupling between the planes, a typical storage ring with no bending of the orbit in the vertical plane will have $D_y = 0$ everywhere.

In addition to dispersion, a particle with $\delta \neq 0$ will also be subject to different focusing than the reference particle. This affects the beta functions for the off-momentum particle, and in turn the tune. Considering only the linear effect of

δ on the tune, the *chromaticity* ξ_u is defined by [7]

$$\Delta Q_u = \delta \xi_u + \mathcal{O}(\delta^2), \tag{2.25}$$

where ΔQ_u is the change in tune for a given δ. Quadrupole fields contribute to the so-called *natural chromaticity*, which is always negative since higher energy particles will be focused less. A large chromaticity is detrimental, since the inherent energy spread of the beam then gives rise to a large *tune spread* which complicates the avoidance of strong resonances. To correct the chromaticity, *sextupole* magnets are used. To first order, the corrected chromaticity is given by

$$\begin{aligned} \xi_x &= -\frac{1}{4\pi} \int_0^C \mathrm{d}s\, \beta_x \left(K_x(s) - k_2(s) D_x(s) \right), \\ \xi_y &= -\frac{1}{4\pi} \int_0^C \mathrm{d}s\, \beta_y \left(K_y(s) + k_2(s) D_x(s) \right). \end{aligned} \tag{2.26}$$

Note that the horizontal dispersion D_x enters the expressions for both ξ_x and ξ_y. Sextupole magnets that are installed with the main goal of correcting chromaticity are called *chromatic* sextupole magnets. To correct for unwanted non-linear effects caused by the chromatic sextupole magnets, *harmonic* sextupole magnets are often installed, which are instead placed in sections with low dispersion where they have minimal impact on the chromaticity.

As will be shown in Section 3.2, the TRIBs optics are very sensitive to the horizontal tune. The horizontal chromaticity must therefore be close to zero, so that the tune spread the off-momentum particles is minimized. A more thorough discussion of the effects of chromaticity for TRIBs can be found in [4].

2.6 Hamiltonian Mechanics

A powerful framework for beam dynamics is *Hamiltonian mechanics*. The state $\mathbf{X}$ of an object (in our case a particle) in a Hamiltonian system is described in terms of generalized coordinates $q_1, \cdots q_n$ with associated canonical momenta $p_1, \cdots, p_n$, which forms a $2n$-dimensional phase space. In accelerator physics, the most straight forward choice of such variables are the coordinates x, y, τ and their respective momenta x', y' and δ (or p_x, p_y and δ). These evolve with respect to a time-like, independent variable t, for example s. The equations of motion in a Hamiltonian system with respect to t is given by [8]

$$\begin{aligned} \frac{\mathrm{d}q_i}{\mathrm{d}t} &= \frac{\partial H}{\partial p_i}, \\ \frac{\mathrm{d}p_i}{\mathrm{d}t} &= -\frac{\partial H}{\partial q_i}, \end{aligned} \tag{2.27}$$

where the *Hamiltonian* of the system is a function $H(\mathbf{X}; t)$ of the particle state and the independent variable. It should be noted that H depends on the choice of coordinate system, as well as the independent variable.

Now consider the action-angle coordinates $(J_x, \phi_x, J_y, \phi_y)$, with ϕ_u as the generalized coordinates q_i. For uncoupled motion, the Hamiltonian with respect to the independent variable s is given by

$$H(J_x, \phi_x, J_y, \phi_y; s) = \frac{J_x}{\beta_x(s)} + \frac{J_y}{\beta_y(s)}. \tag{2.28}$$

Applying Eq. (2.27) then yields the equations of motion

$$\begin{aligned} \frac{\mathrm{d}\phi_u}{\mathrm{d}s} &= \frac{\partial H}{\partial J_u} = \frac{1}{\beta_u} = \frac{\mathrm{d}\mu_u}{\mathrm{d}s}, \\ \frac{\mathrm{d}J_u}{\mathrm{d}s} &= -\frac{\partial H}{\partial \phi_u} = 0, \end{aligned} \tag{2.29}$$

where the definition of the phase advance given in Eq. (2.9) has been used. By integrating this equation from s_0 to s_1, Eq. (2.17) can be recovered.

Now suppose we are only interested in the motion in the horizontal plane. A natural choice for the independent variable, implicitly used in for example [4], is given by

$$t = \frac{\mu_x}{2\pi Q_x}, \tag{2.30}$$

This is a convenient choice since t increases by one each turn. Applying the chain rule, we get

$$\frac{\mathrm{d}\phi_u}{\mathrm{d}t} = \frac{\mathrm{d}\phi_u}{\mathrm{d}s}\frac{\mathrm{d}s}{\mathrm{d}t} = \frac{\beta_x(t)}{\beta_u(t)} 2\pi Q_x. \tag{2.31}$$

Thus, with the independent variable t defined in Eq. (2.30), the Hamiltonian becomes

$$H(J_x, \phi_x, J_y, \phi_y; t) = 2\pi Q_x \left(J_x + \frac{\beta_x(t)}{\beta_y(t)} J_y \right). \tag{2.32}$$

It is clear that this choice of t inherently prioritizes the motion in the horizontal plane. This is desirable since, as will be discussed later in Section 3.2, the TRIBs motion is almost exclusively horizontal. Disregarding the vertical motion completely, the linear Hamiltonian can be simplified to just

$$H(J_x, \phi_x) = 2\pi Q_x J_x, \tag{2.33}$$

since the Hamiltonian is now constant with respect to t.

3 Non-linear Optics

While the equations for transverse linear optics have closed form solutions, there are no general closed form solutions when the effects of higher-order fields such as those from sextupole and octupole magnets are included. Simulations, often called *tracking* in the context of accelerator physics, is therefore an effective method used to predict non-linear behavior. Nevertheless, an analytical approach is often valuable to better understand the underlying phenomena. One such analytical approach to non-linear optics is Hamiltonian mechanics in combination with perturbation theory, where the higher-order fields are treated as perturbations to the linear dynamics discussed in Section 2. It should be noted that the notation used in non-linear optics varies greatly between sources. As one of the main inspirations for the framework used throughout this paper, much of the notation will be adapted to be consistent with [4].

3.1 The Non-resonant Hamiltonian

For now, consider the usual case of a storage ring that is far from any resonance. The transverse Hamiltonian can be expanded as a series over the complex *basis functions* [4, 9]

$$|jklm\rangle = (2J_x)^{(j+k)/2}(2J_y)^{(l+m)/2}e^{i[(j-k)\phi_x+(l-m)\phi_y]}, \tag{3.1}$$

also called *kets*. Any Hamiltonian can then be described by the series

$$H(J_x, \phi_x, J_y, \phi_y) = \sum_{jklm} h_{jklm}\,|jklm\rangle\,. \tag{3.2}$$

Note that in general, the Hamiltonian will vary along the ring. For simplicity, the calculations presented in this section will only consider the Hamiltonian at $s = 0$, as a change of coordinate system will later be used in Section 3.2 to make the Hamiltonian constant over the length of the ring.

The analytic calculation of the *driving terms* h_{jklm} in Eq. (3.2) can be approached in a variety of ways such as Lie Algebra [4] and canonical perturbation theory [5]. Consider a general perturbative approach

$$h_{jklm} = h^{(0)}_{jklm} + h^{(1)}_{jklm} + h^{(2)}_{jklm} + \cdots\,, \tag{3.3}$$

where $h^{(0)}_{jklm}$ is given by the linear optics (see Section 2.6) and each successive correction $h^{(n)}_{jklm}$ is calculated using n:th-order perturbation theory. The usefulness of perturbation theory hinges on the fact that for sufficiently well-behaved problems, higher-order corrections will tend towards zero. This thesis considers driving terms up to second order, the explicit calculations for which will be further explained in the coming subsections. The driving terms h_{jklm} are sometimes normalized by the tunes, yielding the *resonance driving terms*

$$f_{jklm} = \frac{h_{jklm}}{e^{2\pi i[(j-k)Q_x+(l-m)Q_y]} - 1}. \tag{3.4}$$

3.1.1 First-order Perturbation Theory

We now wish to calculate the driving terms $h^{(1)}_{jklm}$ in Eq. (3.3), for now limiting ourselves to the Hamiltonian at $s = 0$. For notational convenience, start by defining the functions

$$\Gamma_{jklm}(s) = -\frac{i^{l+m}\beta_x^{(j+k)/2}\beta_y^{(l+m)/2}}{2^{(j+k+l+m)}\, j!\, k!\, l!\, m!} e^{i[(j-k)\mu_x+(l-m)\mu_y]}, \tag{3.5}$$

which only depend on the CS parameters and phase advance. A normal or skew multipole of order $n-1$ will locally contribute to a first-order driving term according to the selection rule $j+k+l+m = n$ given by [4, 9]

$$G_{jklm}(s) = \begin{cases} k_{n-1}(s)\,\Gamma_{jklm}(s), & l+m \text{ even}, \\ j_{n-1}(s)\,\Gamma_{jklm}(s), & l+m \text{ odd}. \end{cases} \tag{3.6}$$

The first-order driving term $h^{(1)}_{jklm}$ at the position $s = 0$ is then given by integrating the local contributions over the length of the ring

$$h^{(1)}_{jklm} = \int_0^C \mathrm{d}s\, G_{jklm}(s). \tag{3.7}$$

As opposed to other formulations such as [5, 9] which assumes thin multipoles with zero length, this calculation of the driving terms has the benefit of correctly considering the effect of thick multipoles [4].

It should be noted that the Hamiltonian in Eq. (3.2) must always be real valued. We therefore expect any terms h_{jjll} to be real, since $|jjll\rangle = (2J_x)^j(2J_y)^l$ is real. The terms h_{jklm} where $j \neq k$ and $l \neq m$ can, however, be complex valued under the condition $h_{kjml} = h^*_{jklm}$ since

$$\begin{aligned} h_{jklm}\,|jklm\rangle + h_{kjml}\,|kjml\rangle &= h_{jklm}\,|jklm\rangle + h^*_{jklm}\,|jklm\rangle^* \\ &= 2\mathrm{Re}\left[h_{jklm}\,|jklm\rangle\right], \end{aligned} \tag{3.8}$$

where we have used the property $|jklm\rangle = |kjml\rangle^*$ which follows directly from Eq. (3.1). Inspection of Eqs. (3.5) to (3.7) indeed shows that $h^{(1)}_{kjml} = h^{(1)*}_{jklm}$, which also implies $h^{(1)}_{jjll}$ is real. This symmetry will be used throughout the thesis to simplify calculations where appropriate.

Consider the first-order driving terms excited by the normal sextupole magnets in the 1.5 GeV ring, which according to the selection rules for Eq. (3.5) excite all driving terms where $j+k+l+m = 3$ and $l+m$ is even. Excluding terms redundant due to the symmetry shown in Eq. (3.8), we conclude that the normal sextupoles give rise to the first-order driving terms

$$h^{(1)}_{3000},\ h^{(1)}_{2100},\ h^{(1)}_{1011},\ h^{(1)}_{1002} \text{ and } h^{(1)}_{1020}. \tag{3.9}$$

As will be discussed in Section 4, the 1.5 GeV ring does not have any octupole magnets installed. Nevertheless, there are normal octupole contributions due to fringe fields and, as will be shown in Section 4.2.2, the IDs. These instead excite first-order terms $j+k+l+m=4$ where $l+m$ is even. This results in the purely horizontal terms

$$h^{(1)}_{4000},\ h^{(1)}_{3100} \text{ and } h^{(1)}_{2200}, \tag{3.10}$$

the coupled driving terms

$$h^{(1)}_{2020},\ h^{(1)}_{2002},\ h^{(1)}_{2011},\ h^{(1)}_{1120} \text{ and } h^{(1)}_{1111}, \tag{3.11}$$

and the purely vertical driving terms

$$h^{(1)}_{0040},\ h^{(1)}_{0031} \text{ and } h^{(1)}_{0022}. \tag{3.12}$$

The driving terms of the form h_{jjll}, in this case $h^{(1)}_{2200}$, $h^{(1)}_{0022}$ and $h^{(1)}_{1111}$, are called *detuning terms*. Consider, for example, the basis function $|2200\rangle = 4J_x^2$. Note that $\frac{\partial}{\partial J_x}|2200\rangle = 8J_x$ varies with J_x, which according to Eq. (2.28) will result in different rates of phase advance depending on the action. This leads to a tune shift with amplitude, also called *amplitude dependent tune shift* (ADTS).

3.1.2 Second-order Perturbation Theory

The second-order contributions $h^{(2)}_{jklm}$ are more cumbersome to calculate, so, for the sake of brevity, a full derivation or general expression for the second-order driving terms will not be presented here. Instead, the explicit expressions are shown only for relevant second-order driving terms. More detailed treatment of these calculations can mainly be found in [4], or alternatively [5, 9].

As will later be discussed in Section 3.2, only the driving terms h_{3000}, h_{2200}, h_{1111} and h_{0022} are included in the resonant Hamiltonian. A pair of first-order terms related to $|jklm\rangle$ and $|pqrt\rangle$ will contribute to the second order term $h^{(2)}_{abcd}$ according to the selection rules [9]

$$\begin{aligned} a &= j+p-1, & & a = j+p,\\ b &= k+q-1, & & b = k+q,\\ c &= l+r, & \text{or} \quad & c = l+r-1,\\ d &= m+t, & & d = m+t-1,\\ jq-kp &\neq 0, & & lt-mr \neq 0. \end{aligned} \tag{3.13}$$

These selection rules are further motivated in Appendix A. Focusing on the horizontal detuning term h_{2200} and applying the selection rules to the first-order terms driven by normal sextupoles listed in Eq. (3.9), the only combinations of interest are the pairs $|3000\rangle$, $|0300\rangle$ and $|2100\rangle$, $|1200\rangle$. Finally, the second-order contribution $h^{(2)}_{2200}$ can be calculated from these first-order terms according to

$$\begin{aligned} h^{(2)}_{2200} = \; & \mathrm{Im}\Big[18\, f^{(1)}_{0300}\, h^{(1)}_{3000} + 6\, f^{(1)}_{1200}\, h^{(1)}_{2100}\Big] \\ & - \int_0^C \mathrm{d}s\, \mathrm{Im}\Big[18\, G_{0300}(s)\, h^{(1)}_{3000}(s) + 6\, G_{1200}(s)\, h^{(1)}_{2100}(s)\Big]. \end{aligned} \tag{3.14}$$

the proof for which is referred to [4]. Here, the terms $h^{(1)}_{jklm}(s)$ do not refer to the value of $h^{(1)}_{jklm}$ at a position s along the ring, but are instead defined as

$$h^{(1)}_{jklm}(s) = \int_0^s \mathrm{d}s'\, G_{jklm}(s'). \tag{3.15}$$

Note that, except for the upper integration bound s, Eq. (3.15) is identical to Eq. (3.7).

According to the selection rules in Eq. (3.13), the first-order terms from the sextupoles also contribute to $h^{(2)}_{1111}$ and $h^{(2)}_{0022}$. Explicit expressions for these contributions can be found in Appendix A. However, there is no combination of the first-order terms from Eqs. (3.9), (3.10), (3.11) and (3.12) that contribute to h_{3000}, which means that $h^{(2)}_{3000} = 0$.

3.2 The Resonant Hamiltonian

Consider a horizontal tune close to a third-order resonance such that $Q_x = I/3 + d$ for some positive integer I, where $d \ll 1$ is the distance from the resonance. Close to resonance, it is often beneficial to use a rotating reference frame in which a particle with the resonant tune $I/3$ is stationary. A new angle coordinate is therefore defined according to [8]

$$\tilde{\phi}_x = \phi_x - \frac{I/3}{Q_x}\mu_x(s). \tag{3.16}$$

This gives a new set of coordinates $(J_x, \tilde{\phi}_x)$ which will be referred to as the *resonant frame*. Since we are interested in the motion in the horizontal plane, we use the independent variable t defined in Eq. (2.30). In the resonant frame, the linear Hamiltonian in Eq. (2.33) then becomes

$$H(J_x, \tilde{\phi}_x) = 2\pi d J_x. \tag{3.17}$$

The non-resonant framework presented in Section 3.1 is no longer fully valid. The treatment of the non-linear Hamiltonian in the resonant case will not be derived here, but the main results needed for the treatment of TRIBs will be presented. It has been shown that for small enough d, to good approximation, the non-linear Hamiltonian in the horizontal plane can described by [4, 5, 7, 8]

$$
\begin{aligned}
H(J_x, \tilde{\phi}_x) = 2\pi d J_x - h_{2200}\,|2200\rangle - 2\mathrm{Re}\left[h_{3000}\,|3000\rangle\right] \\
- h_{1111}\,|1111\rangle - h_{0022}\,|0022\rangle\,,
\end{aligned}
\tag{3.18}
$$

assuming that the vertical tune is far from resonance. It is important to note that J_y and ϕ_y are excluded as arguments to H even though the right-hand side implicitly depends on J_y, since applying the equations of motion in Eq. (2.27) of this H does not describe the motion in the vertical plane. The vertical motion is instead just considered as a perturbation which introduces a varying term J_y. Also note that the basis functions $|jklm\rangle$ in Eq. (3.18) are implicitly redefined in the resonant frame by substituting ϕ_x with $\tilde{\phi}_x$ in Eq. (3.1) to keep the notation simpler.

Now consider the term $f^{(1)}_{0300}h^{(1)}_{3000}$ in Eq. (3.14) for $Q_x = I/3 + d$. Using the approximation $e^{6\pi i Q_x} = e^{2p\pi i}e^{6\pi i d} \approx 1 + 6\pi i d$, we get

$$
f^{(1)}_{0300}h^{(1)}_{3000} = \frac{|h^{(1)}_{3000}|^2}{e^{-6\pi i Q_x} - 1} \approx -\frac{|h^{(1)}_{3000}|^2}{6\pi i d}. \tag{3.19}
$$

Equation (3.19) is rather troublesome as it suggests that h_{2200} could diverge as $d \to 0$. The behavior of this term is not at all trivial, and cannot be adequately described using non-resonant perturbation theory. It has however been shown using canonical perturbation theory [5] and more recently Lie algebraic techniques [4] that a careful resonant treatment results in a revised detuning parameter given by

$$
\begin{aligned}
\tilde{h}^{(2)}_{2200} = {} & \mathrm{Im}\Big[6\,f^{(1)}_{1200}\,h^{(1)}_{2100}\Big] \\
& - \int_0^C \mathrm{d}s\,\mathrm{Im}\Big[18\,G_{0300}(s)\,h^{(1)}_{3000}(s) + 6\,G_{1200}(s)\,h^{(1)}_{2100}(s)\Big],
\end{aligned}
\tag{3.20}
$$

which is essentially identical to Eq. (3.14) except for the exclusion of the problematic term $f^{(1)}_{0300}h^{(1)}_{3000}$ from Eq. (3.19). The driving terms $h^{(2)}_{1111}$ and $h^{(2)}_{0022}$ are unaffected as $d \to 0$.

With the revised detuning term in Eq. (3.20) in mind, including first- and second-order driving terms from normal sextupole and octupole magnets, the driving terms in Eq. (3.18) are finally given by

$$
\begin{cases}
h_{3000} = h^{(1)}_{3000}, \\
\tilde{h}_{2200} = h^{(1)}_{2200} + \tilde{h}^{(2)}_{2200}, \\
h_{1111} = h^{(1)}_{1111} + h^{(2)}_{1111}, \\
h_{0022} = h^{(1)}_{0022} + h^{(2)}_{0022}.
\end{cases}
\tag{3.21}
$$

3.2.1 The TRIBs Parameters

Replacing h_{2200} with the revised driving term $\tilde{h}_{2200}$ and expanding the basis functions using Eq. (3.1), the Hamiltonian in Eq. (3.18) can be more compactly summarized as

$$\frac{H(J_x, \tilde{\phi}_x)}{2\pi} = dJ_x + \frac{\alpha}{2}J_x^2 + \alpha_{xy}J_xJ_y + \frac{\alpha_{yy}}{2}J_y^2 + |F|J_x^{3/2}\cos(3\tilde{\phi}_x + \chi), \quad (3.22)$$

where the parameters

$$\begin{aligned} \alpha &= -\frac{4}{\pi}\tilde{h}_{2200} \qquad & F &= |F|e^{i\chi} = -\frac{2^{3/2}}{\pi}h_{3000} \\ \alpha_{xy} &= -\frac{2}{\pi}h_{1111} \qquad & \alpha_{yy} &= -\frac{4}{\pi}h_{0022} \end{aligned} \quad (3.23)$$

have been introduced. From now on, the parameters d, α, α_{xy}, α_{yy} and F (or equivalently $|F|$ and χ) will be referred to as TRIBs parameters as they fully describe the Hamiltonian in Eq. (3.22).

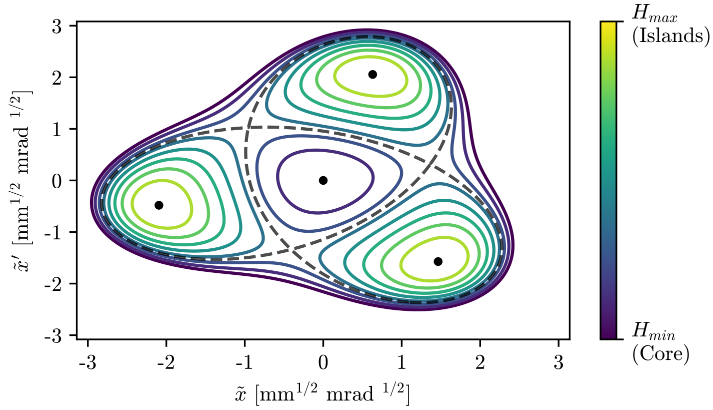

Figure 3.1: Equipotential curves for the Hamiltonian in Eq. (3.24). The color scale indicates the value of the Hamiltonian relative to the minimum at the core and maxima at the islands.

Due to the formation of island orbits in the horizontal plane, it is generally the case that $J_x \gg J_y$. Combined with the limited linear coupling between the planes in a typical storage ring, the coupling terms α_{xy} and α_{yy} can often be neglected yielding the Hamiltonian

$$\frac{H(\phi_x, J_x)}{2\pi} = dJ_x + \frac{\alpha}{2}J_x^2 + |F|J_x^{3/2}\cos(3\tilde{\phi}_x + \chi). \quad (3.24)$$

This Hamiltonian is illustrated in Fig. 3.1, which uses the TRIBs parameters found in Tab. 3.1. Note that the Hamiltonian is at a local minimum at the core, while the island stable fixed points are local maxima.

Table 3.1: The TRIBs parameters of the 1.5 GeV ring at open gaps and the tune $Q_x = 0.3355$, as given by the AT lattice model later described in Section 4.2. The uncertainty is a result of variations in the LOCO measurements.

Parameter	Value	Uncertainty (1σ)
d	$2.17 \cdot 10^{-3}$	N/A
α [m^{-1}]	-1440	7.4
$\lvert F\rvert$ [m$^{-1/2}$]	0.509	0.039
χ [rad]	-2.463	0.088
α_{xy} [m^{-1}]	-9030	2.6
α_{yy} [m^{-1}]	5240	2.9

3.2.2 Stable Fixed Points of the Hamiltonian

Each stable fixed point of the Hamiltonian corresponds to a stable closed orbit around the ring, with the core orbit given by the origin $(J_x, \tilde{\phi}_x) = (0, 0)$. At a fixed point, the partial derivatives of the Hamiltonian with respect to J_x and $\tilde{\phi}_x$ must be zero, which gives

$$\begin{aligned} d + \alpha J_x + \frac{3}{2}|F|\sqrt{J_x}\cos(3\tilde{\phi}_x + \chi) = 0, \\ \sin(3\tilde{\phi}_x + \chi) = 0. \end{aligned} \tag{3.25}$$

The condition $\sin(3\tilde{\phi}_x + \chi) = 0$ corresponds to the two cases $\cos(3\tilde{\phi}_x + \chi) = \pm 1$. The stable fixed points correspond to the case $\cos(3\tilde{\phi}_x + \chi) = 1$, while $\cos(3\tilde{\phi}_x + \chi) = -1$ correspond to unstable fixed points [4]. For the stable fixed points $(J_{\text{SFP}}, \tilde{\phi}_{\text{SFP}})$, it then holds that

$$\begin{aligned} d + \alpha J_{\text{SFP}} + \frac{3}{2}|F|\sqrt{J_{\text{SFP}}} = 0, \\ \cos(3\tilde{\phi}_{\text{SFP}} + \chi) = 1. \end{aligned} \tag{3.26}$$

Using the fact that the first row of Eq. (3.26) is a quadratic equation in $\sqrt{J_{\text{SFP}}}$, it can then be shown for the case $d > 0$, $\alpha < 0$ that [4]

$$\begin{aligned} J_{\text{SFP}} &= \frac{\left(3|F| + \sqrt{9|F|^2 - 16\alpha d}\right)^2}{16\alpha^2}, \\ \tilde{\phi}_{\text{SFP}} &= \frac{2n\pi - \chi}{3}, \end{aligned} \tag{3.27}$$

for an integer n depending on the choice of island bucket.

3.2.3 The Island Tunes

The particles in the island orbit experience a different focusing due to ADTS, leading to difference in tune between the island orbit and core orbit. This effect can be calculated numerically using tracking, but an analytical approach is also desirable. For the sake of clarity, the following derivation of the analytical island tune is limited to the case $d > 0$ and $\alpha < 0$, which is relevant for the TRIBs optics of the 1.5 GeV ring.

Consider the motion of a particle close to the stable fixed point $(J_{\mathrm{SFP}}, \tilde{\phi}_{\mathrm{SFP}})$ of the Hamiltonian in Eq. (3.24). The independent variable for this Hamiltonian is $t = \mu_x/2\pi Q_x$ as defined in Eq. (2.30), which by definition increases by one for each turn around the ring. According to Eq. (2.27), the equations of motion of the resonant Hamiltonian are given by

$$\begin{aligned} J'(t) &= -\frac{\partial H}{\partial \tilde{\phi}_x} = 2\pi \left(3|F|J_x^{3/2}\sin(3\tilde{\phi}_x + \chi)\right), \\ \phi'(t) &= \ \ \frac{\partial H}{\partial J_x} = 2\pi \left(d + \alpha J_x + \frac{3}{2}|F|J_x^{1/2}\cos(3\tilde{\phi}_x + \chi)\right). \end{aligned} \tag{3.28}$$

Considering a Taylor expansion in J_x and $\tilde{\phi}_x$ around the stable fixed point, define $J(t) = J_{\mathrm{SFP}} + \delta J(t)$ and $\tilde{\phi}_x(t) = \tilde{\phi}_{\mathrm{SFP}} + \delta\phi(t)$ for some small offsets $\delta J(t)$ and $\delta\phi(t)$. A first-order Taylor expansion of Eq. (3.28), simplified using the fixed point conditions in Eq. (3.26), then yields

$$\begin{aligned} \delta J'(t) &= 2\pi \left(9|F|J_{\mathrm{SFP}}^{3/2}\right)\delta\phi, \\ \delta\phi'(t) &= 2\pi \left(\frac{3|F|}{4\sqrt{J_{\mathrm{SFP}}}} + \alpha\right)\delta J. \end{aligned} \tag{3.29}$$

While it is clear that the the factor $9|F|J_{\mathrm{SFP}}^{3/2}$ in Eq. (3.29) is positive, the sign of $3|F|/4\sqrt{J_{\mathrm{SFP}}} + \alpha$ is not immediately obvious since $\alpha < 0$. Using the fixed point condition for J_{SFP} from Eq. (3.26), the linear equations of motion in Eq. (3.29) can be rewritten as

$$\begin{aligned} \delta J'(t) &= \ \ 2\pi \left(9|F|J_{\mathrm{SFP}}^{3/2}\right)\delta\phi, \\ \delta\phi'(t) &= -2\pi \left(\frac{3|F|}{4\sqrt{J_{\mathrm{SFP}}}} + \frac{d}{J_{\mathrm{SFP}}}\right)\delta J, \end{aligned} \tag{3.30}$$

which leaves the sign of each term unambiguous for $d > 0$. Combining the two expressions in Eq. (3.30) yields

$$\begin{aligned} \delta\phi''(t) &= -4\pi^2 \cdot 9|F|J_{\mathrm{SFP}}^{3/2}\left(\frac{3|F|}{4\sqrt{J_{\mathrm{SFP}}}} + \frac{d}{J_{\mathrm{SFP}}}\right)\delta\phi(t) \\ &= -(2\pi d_{\mathrm{SFP}})^2\delta\phi(t). \end{aligned} \tag{3.31}$$

This differential equation has a periodic solution with frequency d_{SFP} since $d_{\mathrm{SFP}}^2 > 0$. Since the independent variable t of the Hamiltonian denotes the number of turns, it is clear that d_{SFP} is the tune of the islands in the resonant frame.

The sign of d_{SFP} with respect to the tune Q_x, i.e. the direction of motion in the resonant frame compared to the overall betatron motion, can be determined from Eq. (3.30). Alternatively, inspection of the Hamiltonian equations of motion defined in Eq. (2.27) makes it clear that a sign change in H corresponds to all motion being reversed. Since the stable fixed point in the core is a local minimum while the stable fixed points in the islands are local maxima, the direction of rotation in the islands must be opposite to that of the core. Thus, d_{SFP} must have the opposite sign of d. For $d > 0$, it can finally be concluded from Eq. (3.31) that

$$d_{\mathrm{SFP}} = -\frac{3}{2}\sqrt{3|F|^2 J_{\mathrm{SFP}} + 4d|F|\sqrt{J_{\mathrm{SFP}}}}. \tag{3.32}$$

Taking into account that this motion occurs in the resonant frame $(J_x, \tilde{\phi}_x)$, the total betatron tune in the islands is given by

$$Q_{x,\mathrm{SFP}} = \frac{I}{3} + d_{\mathrm{SFP}}, \tag{3.33}$$

which implies that the island tunes must be below resonance for $d > 0$ and $\alpha < 0$.

3.2.4 Efficient Numerical Computation of TRIBs Parameters

As will later be discussed in Section 6, the compensation of IDs relies on numerical optimization of the TRIBs parameters using sextupole corrections. To this end, a novel formulation for calculating the TRIBs parameters is presented, which allows for efficient calculation of the TRIBs parameters when non-linear magnets are varied while the linear optics is fixed. Since both the beta functions and phase advances are independent of sextupole and octupole distribution, the dependence of the parameters on integrals over the linear optics can be separated from the dependence on the sextupole and octupole distribution. This allows for efficient numerical computation of driving terms using sums similar to thin-lens calculations such as in [5,9], without the associated loss of accuracy due to the thin-lens approximation.

Assume a piecewise constant normal multipole distribution, as is often the case for a lattice model. Skew multipoles are not considered. For each element $0 \le u \le N$, we define the multipole strengths

$$k_n(s) = k_n^{(u)}, \quad s_u < s < s_{u+1}, \tag{3.34}$$

where s_u and s_{u+1} are the start- and endpoints of the element. The first-order term $h^{(1)}_{jklm}(s)$, which depends on $k_{n_j}(s)$ where $n_j = j + k + l + m - 1$, can then be calculated according to

$$\begin{aligned} h^{(1)}_{jklm}(s_{u+1}) &= \sum_{v=0}^{u} k_{n_j}^{(v)} \mathcal{G}^{(v)}_{jklm}, \\ \mathcal{G}^{(u)}_{jklm} &= \int_{s_u}^{s_{u+1}} \mathrm{d}s\, \Gamma_{jklm}(s) ds, \end{aligned} \tag{3.35}$$

where each value of $k_{n_j}^{(u)}$ has been factored out from the integral in Eq. (3.7).

A similar approach can be employed also for second order terms $h_{abcd}^{(2)}$. Equations (3.20), as well Eqs. (A.4) and (A.5) from Appendix A, all involve terms of the form

$$\begin{aligned} \int_0^C \mathrm{d}s\, G_{pqrt}(s)\, h_{jklm}^{(1)}(s) &= \int_0^C \mathrm{d}s \int_0^s \mathrm{d}s'\, k_{n_p}(s)\, \Gamma_{pqrt}(s)\, k_{n_j}(s)\, \Gamma_{jklm}(s') \\ &= \sum_{\substack{u,v \\ u>v}} k_{n_p}^{(u)} k_{n_j}^{(v)} \mathcal{G}_{pqrt}^{(u)} \mathcal{G}_{jklm}^{(v)} \\ &+ \sum_{u} k_{n_j}^{(u)} k_{n_p}^{(u)} \int_{s_u}^{s_{u+1}} \mathrm{d}s \int_{s_u}^{s} \mathrm{d}s'\, \Gamma_{pqrt}(s) \Gamma_{jklm}(s'), \end{aligned} \tag{3.36}$$

where $n_p = p+q+r+t-1$ is used to differentiate from n_j. Note that Eq. (3.36) is a quadratic form which can be more compactly written as

$$\begin{aligned} \int_0^C \mathrm{d}s\, G_{pqrt}(s) h_{jklm}^{(1)}(s) &= \sum_{u,v} k_{n_p}^{(u)} \mathcal{G}^{A\,(uv)}_{\substack{jklm \\ pqrt}} k_{n_j}^{(v)}, \\ \mathcal{G}^{A\,(uv)}_{\substack{jklm \\ pqrt}} &= \begin{cases} \mathcal{G}_{pqrt}^{(u)} \mathcal{G}_{jklm}^{(v)}, & u > v, \\ \displaystyle\int_{s_u}^{s_{u+1}} \mathrm{d}s \int_{s_u}^{s} \mathrm{d}s'\, \Gamma_{pqrt}(s)\, \Gamma_{jklm}(s'), & u = v, \\ 0, & u < v. \end{cases} \end{aligned} \tag{3.37}$$

Now consider the terms $f_{pqrt} h_{jklm}$ in Eqs. (3.20), (A.4) and (A.5). These can be expressed in the form

$$\begin{aligned} f_{pqrt} h_{jklm} &= \frac{1}{e^{i[(p-q)Q_x + (l-m)Q_y]}} \int_0^C \mathrm{d}s\, G_{pqrt}(s) \int_0^C \mathrm{d}s'\, G_{jklm}(s') \\ &= \frac{1}{e^{i[(p-q)Q_x + (l-m)Q_y]}} \sum_{u,v} k_{n_j}^{(u)} k_{n_p}^{(v)} \mathcal{G}_{jklm}^{(u)} \mathcal{G}_{pqrt}^{(v)}. \end{aligned} \tag{3.38}$$

Similarly to Eq. (3.37), Eq. (3.38) is also a quadratic form which can be written as

$$\begin{aligned} f_{pqrt} h_{jklm} &= \sum_{u,v} k_{n_j}^{(u)} \mathcal{G}^{B\,(uv)}_{\substack{jklm \\ pqrt}} k_{n_p}^{(v)}, \\ \mathcal{G}^{B\,(uv)}_{\substack{jklm \\ pqrt}} &= \frac{\mathcal{G}_{pqrt}^{(v)} \mathcal{G}_{jklm}^{(u)}}{e^{i[(p-q)Q_x + (l-m)Q_y]}}. \end{aligned} \tag{3.39}$$

The parameters F and α Eq. (3.24) are particularly interesting in the case of TRIBs. These can now be elegantly summarized using Eqs. (3.37) and (3.39) into

$$
\begin{aligned}
F &= \sum_u k_2^{(u)} \mathcal{G}_F^{(u)}, \\
\alpha &= \sum_{u,v} k_2^{(u)} \mathcal{G}_\alpha^{(uv)} k_2^{(v)} + \sum_u k_3^{(u)} \mathcal{G}_\alpha^{(u)}
\end{aligned}
\tag{3.40}
$$

where the coefficients in (3.40) are given by

$$
\begin{aligned}
\mathcal{G}_F^{(u)} &= -\frac{2^{3/2}}{\pi} \mathcal{G}_{3000}^{(u)}, \\
\mathcal{G}_\alpha^{(uv)} &= -\frac{4}{\pi} \mathrm{Im}\left[6\mathcal{G}_{\substack{2100\\1200}}^{B\,(uv)} - 18\mathcal{G}_{\substack{3000\\0300}}^{A\,(uv)} - 6\mathcal{G}_{\substack{2100\\1200}}^{A\,(uv)}\right], \\
\mathcal{G}_\alpha^{(u)} &= -\frac{4}{\pi} \mathcal{G}_{2200}^{(u)}.
\end{aligned}
\tag{3.41}
$$

As mentioned in Section 2.5, the chromaticities are also of interest. The contribution of the sextupoles to the chromaticity can be expressed in a similar form, yielding

$$
\begin{aligned}
\xi_x &= -\frac{1}{4\pi} \int_0^C \mathrm{d}s\, \beta_x(s) K_x(s) + \sum_u k_2^{(u)} \mathcal{G}_{\xi x}, \\
\xi_y &= -\frac{1}{4\pi} \int_0^C \mathrm{d}s\, \beta_y(s) K_y(s) + \sum_u k_2^{(u)} \mathcal{G}_{\xi y}.
\end{aligned}
\tag{3.42}
$$

where

$$
\begin{aligned}
\mathcal{G}_{\xi x}^{(u)} &= \int_{s_u}^{s_{u+1}} \mathrm{d}s\, \beta_x(s) D_x(s), \\
\mathcal{G}_{\xi y}^{(u)} &= -\int_{s_u}^{s_{u+1}} \mathrm{d}s\, \beta_y(s) D_x(s).
\end{aligned}
\tag{3.43}
$$

Note that the coefficients $\mathcal{G}^{(u)}$ and $\mathcal{G}^{(uv)}$ do not depend on k_{n_j} and k_{n_p}. This allows them to be calculated only once, under the assumption that the linear optics are not changed. Numeric calculations are further aided by the fact that Eqs. (3.40) and (3.42) can be expressed as matrix operations. Additionally, the derivatives with respect to each $k_2^{(u)}$ of the TRIBs parameters and chromaticity are now trivial to calculate from Eqs. (3.40) and (3.42), which yields

$$
\begin{aligned}
\frac{\partial \alpha}{\partial k_2^{(u)}} &= \sum_v \left(\mathcal{G}_\alpha^{(uv)} + \mathcal{G}_\alpha^{(vu)}\right) k_2^{(v)}, &\qquad \frac{\partial \xi_x}{\partial k_2^{(u)}} &= \mathcal{G}_{\xi x}^{(u)}, \\
\frac{\partial F}{\partial k_2^{(u)}} &= \mathcal{G}_F^{(u)}, & \frac{\partial \xi_y}{\partial k_2^{(u)}} &= \mathcal{G}_{\xi y}^{(u)}.
\end{aligned}
\tag{3.44}
$$

4 The MAX IV 1.5 GeV Storage Ring

The 1.5 GeV ring has a circumference $C = 96\,\text{m}$ which for the RF frequency $f_{RF} = 100\,\text{MHz}$ yields a harmonic number $h = 32$. The ring is composed of 12 near-identical sections called *achromats*, so-called because of their design which enables the horizontal dispersion to vanish in the straight sections in-between each pair of achromats. These straight sections house the IDs for the five user beamlines Bloch, FinEstBeAMS, FlexPES, MAXPEEM, and SPECIES. In addition, the straight sections contain the injection straight (where $s = 0$ is defined) and the RF cavities.

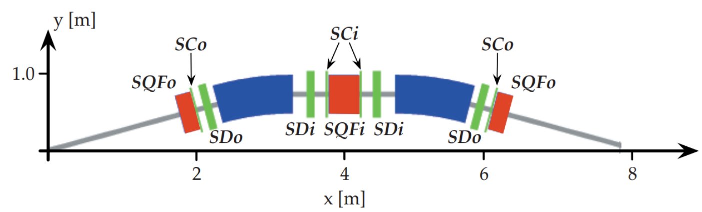

Figure 4.1: Illustration of an achromat in the 1.5 GeV ring showing dipoles (blue), combined-function quadrupoles and sextupoles (red) and pure sextupoles (green). The sextupole families SDo and SDI are controlled globally, while SCI are controlled on a per-achromat basis and SCo on a per-magnet basis. Figure taken from [2].

The achromats in the 1.5 GeV ring make use of numerous combined-function magnets, for example the combined-function quadrupole and sextupole magnet family SQFo. In addition to the combined-function magnets, each achromat is equipped with four families of pure sextupoles named SDo, SDi, SCi and SCo [2]. The magnet families SDo and SDi are connected to one global power supply per family, which means that the sextupole strength k_2 of these families can only be adjusted globally. In contrast, the corrector sextupoles SCo can be adjusted individually (a total of 24 power supplies) while SCi are adjusted on a per-achromat basis (12 power supplies). This gives a total of 38 degrees of freedom for the sextupole configuration. The ring is not equipped with any corrector octupole magnets.

The TRIBs optics studied are based upon the first TRIBs optics as described in [3] which was later refined during the user test week [6]. The TRIBs optics of the 1.5 GeV ring differs from the nominal optics in a few key ways. Firstly, the tune setpoint must be close to a third-order resonance. For this thesis, the tune working point was chosen to be $(Q_x, Q_y) = (11.3355, 3.15)$, corresponding to a distance $d \approx 2.17 \cdot 10^{-3}$ to the resonance $Q_x = 34/3$. As mentioned in Section 2.5, the horizontal chromaticity is also of interest. The chromaticity for the current TRIBs optics were measured to $(\xi_x, \xi_y) = (0.03, 3.34)$.

4.1 Insertion Devices

The IDs are composed of alternating rows of permanent dipole magnets above and below the electron beam orbit. These magnets cause the beam to undulate in the transverse direction, emitting a narrow beam of synchrotron radiation. The main method of adjusting the properties of the emitted radiation is to mechanically adjust the vertical gap between the alternating rows of magnets, thus changing the magnetic field strength and therefore the amplitude of the beam undulation. Adjusting the gap is used to vary the wavelength of the emitted radiation. In addition, some insertion devices have additional degrees of freedom such as the *helical phase*, which allows for adjustment of the polarization of the emitted radiation [10]. As will be further motivated in Section 4.2, only the *planar* ID mode is considered, where the helical phase is zero and the undulation of the electrons resides purely in a single plane.

As the gap of an ID is closed, the magnetic field strength increases which also changes the impact on the motion of the beam. The IDs for Bloch and FinEstBeAMS have a particularly large effect on the beam dynamics, and are therefore fitted with electromagnetic trim wires called *ID compensation strips* that can be used to somewhat compensate for the effect of the ID on the beam. A compensation scheme for these two IDs has been developed for the nominal, non-TRIBs optics, consisting of a *feedforward* device which applies precomputed corrections to the ID compensation strips and the flanking sextupoles [11]. This pre-existing feedforward device, while effective for the non-TRIBs optics, has been found to be insufficient for correction of the TRIBs optics.

4.2 Lattice Modeling in Accelerator Toolbox

All tracking and calculations of linear optics were done using Accelerator Toolbox (AT) in either Python [12] or MATLAB [13]. The AT lattice was based on the standard lattice for the 1.5 GeV ring [14], adjusted to the chosen working tunes.

Tracking can be used to numerically plot the equipotential curves of the Hamiltonian in what is known as a *Poincaré section.* This is done by tracking a number of particles for different starting conditions over a large number of turns, and drawing a scatter plot of the particles phase space coordinates at a particular position along the ring for each turn. Such a Poincaré section is compared to the analytical Hamiltonian in Fig. 4.2.

As Fig. 4.2 shows, the non-linear dynamics are captured very well by the analytical Hamiltonian at lower amplitudes. However, the discrepancies between the analytical Hamiltonian and Poincaré section increase with amplitude, as is expected for any perturbative approach. This discrepancy notably leads to a

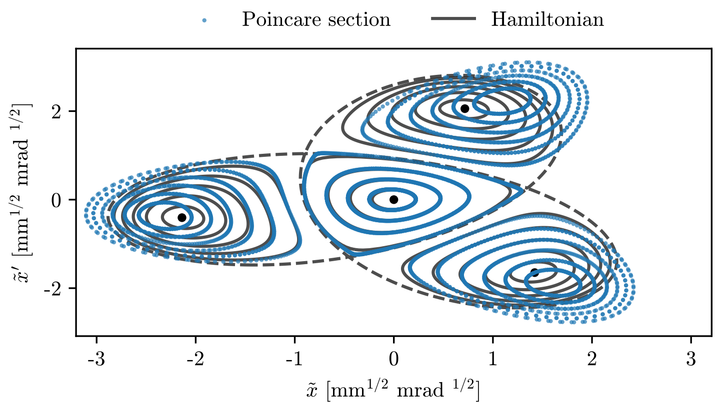

Figure 4.2: A comparison in normalized phase space between a Poincaré section and analytical Hamiltonian of the AT lattice .

larger island orbit amplitude in the Poincaré section. Two additional effects, which cannot be reproduced with a Hamiltonian of the form in Eq. (3.24), can also be observed. Firstly, the stable fixed points of the AT lattice differ slightly in their actions $J_{\mathrm{SFP},n}$. In addition, as opposed to the Hamiltonian where the phase advance of the three island orbits are precisely $2\pi/3$ rad apart, the relative phase advance between the islands of the Poincaré section varies slightly. These additional effects are also seen in measurements, as will be discussed in Section 5.3.

4.2.1 LOCO Measurements

The linear optics and dispersion functions of the lattice were further adjusted using LOCO [15]. A LOCO measurement, among other things, is used to estimate the difference between the design beta functions and the actual beta functions in the machine. This difference, which arises due to field errors, is called *beta beating*. A LOCO fit is used to adjust the quadrupole strengths of the AT lattice to match the measured linear optics as closely as possible. As shown in Eq. (3.5), this beta beating will result in a change of the non-linear resonance terms.

At least one LOCO measurement was taken during each beamtime shift, in order to account for differences in machine condition due to thermal effects and imperfections in the *cycling* of the magnets. Cycling is a process with the goal of minimizing the impact of *magnetic hysteresis*, where the exact field strength of an electromagnet in the ring depends on the recent history of the excitation current [16]. These LOCO measurements are done with fully open ID gaps and the standard sextupole settings for the TRIBs mode. For all comparisons between measurements and theory or tracking, a LOCO measurement from the

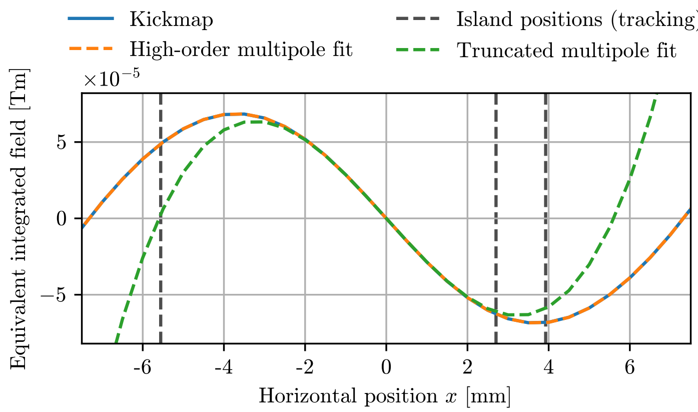

Figure 4.3: A comparison between the equivalent integrated field $B_y(x)$ of the kickmap, high-order multipole fit and the truncated multipole fit for FinEstBeAMS at a gap of 25 mm.

same beamtime shift is used to fit the AT lattice.

4.2.2 Modeling of Insertion Devices

The effects of the IDs Bloch and FinEstBeAMS are typically modeled using *kickmaps* based on simulations in RADIA [17,18]. The kickmaps allow precomputed kicks to be applied during tracking, based on the transverse position of each particle. To incorporate the effects of the IDs into the non-linear Hamiltonian, the kickmaps are approximated by fitting a high-order multipole expansion (up to a_{15} and b_{15}) that results in the same kick for on-momentum particles. Higher-order contributions (decapole fields and higher) were neglected to conform to the theory in Section 3.2. These multipole fits are inserted into the AT lattice in the center of the corresponding ID straights as relatively thin ($L = 0.05$ m) multipole elements.

It was found that for the planar mode, the equivalent multipole expansion does not contain any skew components nor any normal multipole components of even degree b_{2n} such as dipole-, sextupole- and decapole components. This leaves only quadrupole- and octupole- components in the truncated multipole expansion, with the lowest non-negligible order that was discarded being the dodecapole component b_5. And example multipole expansion fit and the effects of the truncation is shown in Fig. 4.3. The resulting quadrupole- and octupole components for FinEstBeAMS and Bloch at different gaps are shown in Fig. 4.4, demonstrating a steep increase of the magnetic field strengths as the minimum gap of 14 mm is approached. The non-planar ID modes are not considered in this thesis as they result in skew multipole components, which are not currently

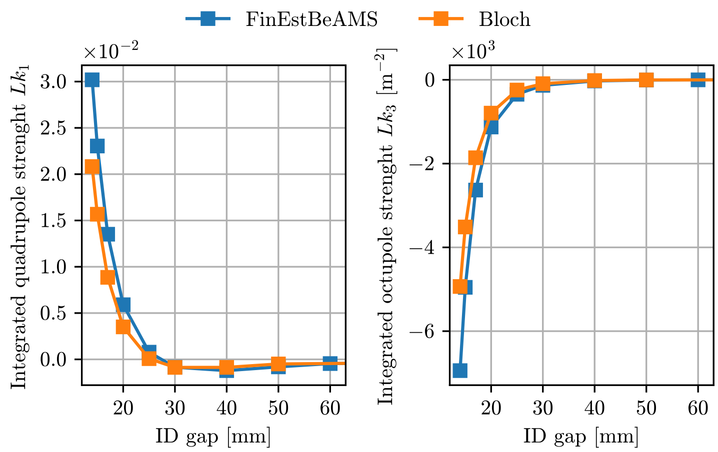

Figure 4.4: The equivalent integrated quadrupole- and octupole strengths as a function of gap for FinEstBeAMS and Bloch.

included in the analysis in Section 3.

4.2.3 Tune Adjustment

The error in tune between the machine and the LOCO fit is negligible for the usual, non-TRIBs, optics at MAX IV. For the TRIBs optics, however, a relative error of just 0.01 % in the horizontal tune Q_x (roughly corresponding to the standard error seen in practice) could increase the distance d to resonance by around 50 %. After the LOCO fit, the tunes of the AT lattice are therefore adjusted to the measured values. To mimic the tune feedback system used on the actual machine as closely as possible, the same magnets are used when adjusting the tune of the AT lattice.

In the actual machine, the focusing effect of the IDs causes a tune shift, which is then compensated for by the tune feedback system. While this correction results in the correct tune, a beta beating arises when such a local perturbation is compensated by a global correction. In AT, this beta beating is estimated by analogously inserting the multipole fit of the ID kickmaps described in Section 4.2.2 into the AT lattice, then adjusting the tune of the lattice as described above.

5 Measurements of TRIBs Orbits at MAX IV

The goal of this section is to introduce the different measurement techniques used to characterize the TRIBs in the 1.5 GeV storage ring. This will allow comparison between measurements and both the analytical framework presented in Section 3.2 and tracking based on the AT lattice described in Section 4.2. Note that hats ($\hat{}$) will be used to indicate measured or estimated quantities.

Most of the observables used throughout are measured using very common techniques, which will be described only briefly for completeness An exception is the island positions which are determined using optical imaging, which can then be used to reconstruct the island orbits in phase space and action-angle coordinates. This procedure is detailed separately in Section 5.1.

The tunes are measured using a *Bunch-by-Bunch* (BbB) device, which is fast enough to measure the transverse positions of each bunch separately. The tune measurement requires a coherent excitation of the betatron oscillations in both planes, achieved using a transverse stripline kicker that is driven over two frequency ranges, each centered around the horizontal and vertical betatron tunes [3]. This is used to measure both core and island tunes yielding $\hat{d}$ and $\hat{d}_{\mathrm{SFP}}$, as shown in Fig. 5.1. The chromaticities $\hat{\xi}_u$ can be measured by recording the change in tunes while scanning over a small range of RF frequencies to change the beam energy.

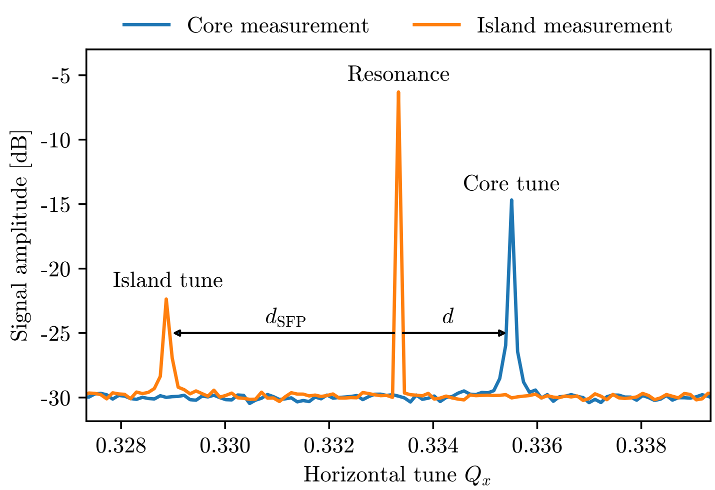

Figure 5.1: An example of two separate measurements of the horizontal core and islands tunes. In addition to the island tune, the island orbits give rise to a strong resonance peak.

Table 5.1: Estimated source point positions s_A and s_B.

Position	Lower bound	Mean	Upper bound	Uncertainty span
$\mathbf{s_A}$ [m]	34.325	34.338	34.351	0.013
$\mathbf{s_B}$ [m]	34.814	34.323	34.833	0.0095

To drive the electrons in a bunch between the core and island orbits, the same stripline kickers used for tune readback are utilized [3]. The core orbit can be depopulated by strongly exciting around the horizontal core tune, thereby populating the island orbits. The opposite holds for driving the electrons to the core, where the island tune is strongly excited to depopulate the islands.

5.1 Imaging Using Diagnostic Beamlines

The SR given off in one of the dipole bends is continuously imaged by two diagnostic beamlines, enabling the parasitic measurement of the transverse distribution of the beams at two source points. In each diagnostic beamline, the synchrotron light is directed by a number of mirrors then focused by a lens onto a CCD sensor. The angular acceptance of the imaging system is controlled by two movable baffles that block unwanted light. The longitudinal position of the two source points A and B are denoted s_A and s_B.

These positions, detailed in Tab. 5.1, have been estimated from the geometry of the beamline assembly and the current position of the baffles. This gives a lower and upper bound for the longitudinal positions s_A and s_B. The final estimates are given by the average of the two bounds, with the uncertainty given by half the interval length.

5.1.1 Reconstruction of Island Orbits

Using the images from the diagnostic beamlines, the positions of the islands can be estimated. The scaling factor from the pixel coordinates to real coordinates is determined by the magnification of the optical system and the physical size of the pixels of the camera sensor. The magnification was measured for an up-to-date calibration, as described in Appendix B.

While the magnification is known, the transverse offset between the imaging plane and the reference orbit is not. The positions of the islands are therefore always measured relative to the core orbit by taking images of both the core and islands. This yields the measured relative positions $\hat{u}_{A,n}$ and $\hat{u}_{B,n}$ of island orbits $n = 1$, 2 and 3 at source points A and B.

The orbit positions are measured by fitting a two-dimensional Gaussian distribution to the image intensity values, one for each orbit. The measured positions are then given by the centroid of the distribution fit. Figure 5.2 shows an im-

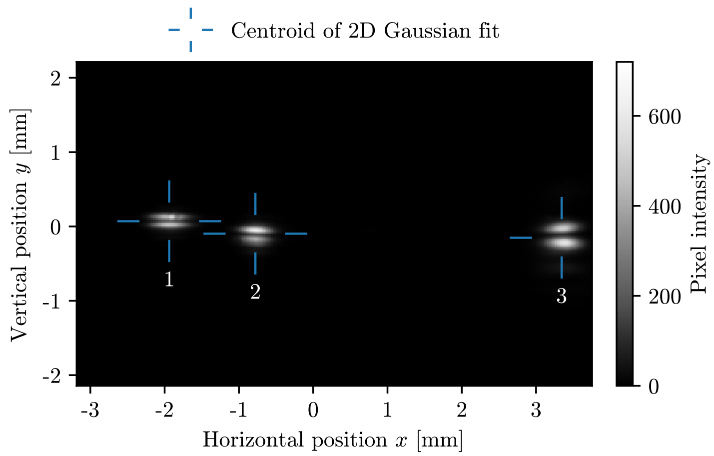

Figure 5.2: An image from diagnostic beamline A, with the centroid of the two-dimensional Gaussian fits overlaid. The island numbering is consistent throughout relevant figures.

age from diagnostic beamline A together with the results from the Gaussian distribution fits.

To reconstruct the phase space correctly, the measured island positions must be correctly matched in pairs $(x_{A,i}, x_{B,i})$ that correspond to the same island bucket. Due to the high agreement between tracking in AT and measurements, the relative order of the islands at the two source points are assumed to be the same as in tracking, where it holds that $x_{A,1} < x_{A,2} < x_{A,3} \Rightarrow x_{B,2} < x_{B,1} < x_{B,3}$. Note the ordering of the horizontal positions at s_A, as this numbering will be used throughout relevant figures to uniquely identify the different island orbits. Using this pairing, the phase space location of the n:th island orbit at s_A can be reconstructed using

$$\hat{u}'_{A,i} = \frac{\hat{u}_{B,i} - m_{11}^{(n)} \hat{u}_{A,i}}{m_{12}^{(n)}}, \tag{5.1}$$

where the elements $m_{ij}^{(u)}$ of the transfer matrix $\mathbf{M}_{s_A \to s_B}$ are defined in Eq. (2.12). An example of such a reconstruction is illustrated in Fig. 5.4, which shows good agreement with both theory and tracking. Note that s_A is relatively close to the entrance of the bending dipole, leading to non-linear fringe fields not modeled by the linear transformation $\mathbf{M}_{s_A \to s_B}$. These are assumed to be negligible over the short distance between the source points, which has also been confirmed using tracking. The island positions can then be expressed in $\hat{J}_x$ and $\hat{\phi}_x$ using Eqs. (2.14) and (2.16), given the CS parameters at s_A. It was found that the average action J_x of the islands was about 50 times the average action J_y. This shows that the horizontal dynamics dominate, further motivating the purely horizontal treatment in Eq. (3.24).

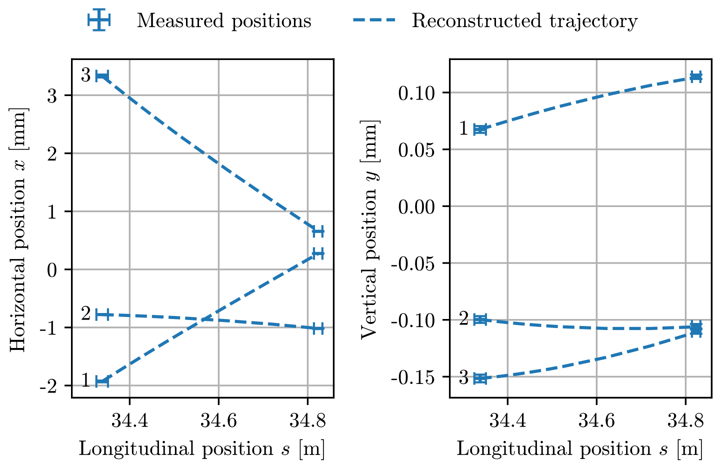

Figure 5.3: The measured positions of the islands at the two diagnostic beamlines for $n = 10$, together with the reconstructed orbits resulting from Eq. (5.1). The uncertainty in s is taken from Tab. 5.1. The island numbering is consistent throughout relevant figures.

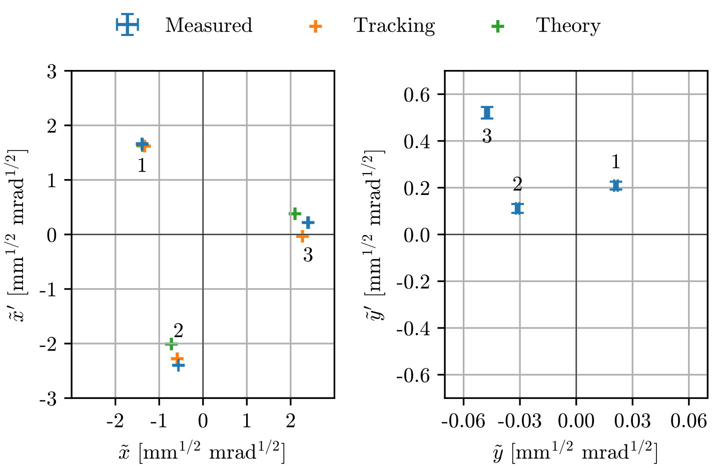

Figure 5.4: The measured normalized phase space coordinates at diagnostic beamline A, compared with both tracking and theory in the horizontal plane. The island numbering is consistent throughout relevant figures.

5.2 Experimental Measurement of TRIBs Parameters

Two different techniques to experimentally determine the TRIBs parameters α and $|F|$ have been developed and are presented in Sections 5.2.1 and 5.2.2. A separate technique required to estimate χ is detailed in Section 5.2.3. This is not only of interest to compare with analytical calculations, but also to evaluate the effectiveness of the ID compensation scheme that will later be introduced in Section 6. It should be noted that other experimental techniques to measure driving terms already exist, such as spectral analysis of Turn-by-Turn (TbT) measurements [9, 19, 20].

5.2.1 The Tune Scan Technique

Using a few assumptions, a tune scan can be used to estimate α and $|F|$. The basic premise is that for a single measurement of $\hat{d}$ and $\hat{J}_{\mathrm{SFP}}$, in this case using the tune readback and the diagnostic beamlines according to Section 5.1.1, there are multiple possible pairs of values for α and $|F|$ that satisfy Eq. (3.27). However, the rate of change $J'_{\mathrm{SFP}} = \frac{\mathrm{d}J_{\mathrm{SFP}}}{\mathrm{d}d}$ of the island action also depends on α and $|F|$. It is therefore possible to estimate α and $|F|$ given both J_{SFP} and J'_{SFP}. The island action is measured over a range of tunes centered at d_{center}, given by the value of d at the nominal tune setpoint specified in Section 4.2.

The values for J_{SFP} and J'_{SFP} are estimated by fitting a linear function $J_{\mathrm{SFP}}(d) = J_{\mathrm{SFP}} + (d - d_{\mathrm{center}})J'_{\mathrm{SFP}}$ to the measurements. Since the island orbits have different actions $J_{\mathrm{SFP},\,n}$, the mean island action $\hat{J}_{\mathrm{SFP}} = (\hat{J}_{SFP,1} + \hat{J}_{SFP,2} + \hat{J}_{SFP,3})/3$ is used. Since both the independent variable $\hat{d}$ and the dependent variable $\hat{J}_{\mathrm{SFP}}$ are measured quantities, with similar levels of uncertainty, an *orthogonal distance regression* (ODR) [21] is used to do a chi-squared fit which correctly takes into account both uncertainties. An example of such a measurement is shown in Fig. 5.5, with notably good agreement between measurement, tracking and theory.

It now remains to estimate α and $|F|$ given the estimates $\hat{J}_{\mathrm{SFP}}$ and $\hat{J}'_{\mathrm{SFP}}$. To first order, the rate of change J'_{SFP} of the island action in Eq. (3.27) as we scan over the tune is given by

$$J'_{\mathrm{SFP}} = \frac{\mathrm{d}J_{\mathrm{SFP}}}{\mathrm{d}d} = \frac{\partial J_{\mathrm{SFP}}}{\partial d} + \frac{\partial J_{\mathrm{SFP}}}{\partial \alpha}\frac{\mathrm{d}\alpha}{\mathrm{d}d} + \frac{\partial J_{\mathrm{SFP}}}{\partial |F|}\frac{\mathrm{d}|F|}{\mathrm{d}d}. \tag{5.2}$$

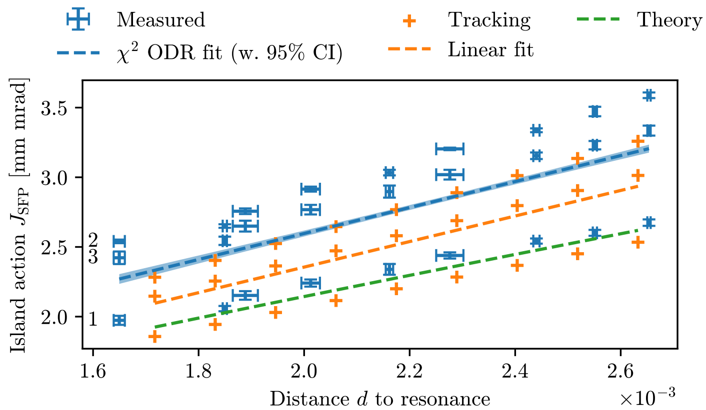

Figure 5.5: An example of the results from a tune scan, compared to tracking and theory. The island numbering is consistent throughout relevant figures.

The partial derivatives Eq. (5.2) of J_{SFP} as given by (3.27), are

$$
\begin{aligned}
\frac{\partial J_x}{\partial d} &= -\frac{1}{\alpha} - \frac{3|F|}{\alpha\sqrt{9|F|^2 - 16\alpha d}},\\
\frac{\partial J_x}{\partial \alpha} &= \frac{4\alpha d - 9|F|^2}{4\alpha^3} + \frac{36\alpha d|F| - 27|F|^3}{4\alpha^3\sqrt{9|F|^2 - 16\alpha d}},\\
\frac{\partial J_x}{\partial |F|} &= \frac{9|F|}{4\alpha^2} + \frac{27|F|^2 - 24\alpha d}{4\alpha^2\sqrt{9|F|^2 - 16\alpha d}}.
\end{aligned}
\tag{5.3}
$$

The derivatives $\frac{\mathrm{d}\alpha}{\mathrm{d}d}$ and $\frac{\mathrm{d}|F|}{\mathrm{d}d}$ in Eq. (5.2) depend on the lattice as well as how the change in tune is achieved, and are therefore not feasible to calculate analytically. They are instead approximated numerically by calculating the TRIBs parameters of the AT lattice over a range of tunes, adjusting the tunes as described in Section 4.2.3.

For measured values $\hat{J}_{\mathrm{SFP}}$ and $\hat{J}'_{\mathrm{SFP}}$, estimates $\hat{\alpha}$ and $|\hat{F}|$ can be found using numerical optimization according to

$$
(\hat{\alpha}, |\hat{F}|) = \underset{\alpha, |F|}{\operatorname{argmin}} \left(\frac{J_{\mathrm{SFP}}(\alpha, |F|) - \hat{J}_{\mathrm{SFP}}}{\hat{J}_{\mathrm{SFP}}} \right)^2 + \left(\frac{J'_{\mathrm{SFP}}(\alpha, |F|) - \hat{J}'_{\mathrm{SFP}}}{\hat{J}'_{\mathrm{SFP}}} \right)^2 \tag{5.4}
$$

where $J_{\mathrm{SFP}}(\alpha, |F|)$ is calculated using Eq. (3.27) and $J'_{\mathrm{SFP}}(\alpha, |F|)$ using Eqs. (5.2) and (5.3). The normalization factors in the denominators are not strictly needed, but help with numerical stability. During the optimization in Eq. (5.4), both $\frac{\mathrm{d}\alpha}{\mathrm{d}d}$ and $\frac{\mathrm{d}|F|}{\mathrm{d}d}$ are assumed to be constant and equal to the numerical approximation obtained from the AT lattice at d_{center}.

5.2.2 The Island Tune Technique

The TRIBs parameters α and $|F|$ can, alternatively, be estimated at a single tune. Squaring both sides of Eq. (3.32) and rearranging yields a quadratic equation in $|F|$ that does not depend explicitly on α

$$\frac{27J_{\mathrm{SFP}}}{4}|F|^2 + 9d\sqrt{J_{\mathrm{SFP}}}|F| - d_{\mathrm{SFP}}^2 = 0. \tag{5.5}$$

Let $\hat{J}_{\mathrm{SFP}}$, $\hat{d}$ and $\hat{d}_{\mathrm{SFP}}$ be measurements of the island action and the core and island tunes, respectively. Since one of the roots is negative, Eq. (5.5) gives the uniquely defined estimate

$$|\hat{F}| = \frac{2\sqrt{\hat{d}^2 + \hat{d}_{\mathrm{SFP}}^2/3} - 2\hat{d}}{3\sqrt{\hat{J}_{\mathrm{SFP}}}}, \tag{5.6}$$

of the resonance strength. Once the estimate $|\hat{F}|$ is obtained from Eq. (5.6), the detuning parameter α can be estimated from the fixed point conditions in Eq. (3.26), which gives

$$\hat{\alpha} = -\frac{\hat{d}}{\hat{J}_{\mathrm{SFP}}} - \frac{3|\hat{F}|}{2\sqrt{\hat{J}_{\mathrm{SFP}}}}. \tag{5.7}$$

This method has the advantage of being considerably simpler to implement than the tune scan technique, while being less invasive since the optics can be left untouched.

The island tune technique was applied to the data already gathered during tune scans. This meant that the island tune $\hat{d}_{\mathrm{SFP}}$ could be estimated by means of a linear ODR chi-squared fit of $d_{\mathrm{SFP}}(d)$, the island tune as a function of core tune. The value and uncertainty of this linear fit at d_{center} is then used. Such a measurement is illustrated in Fig. 5.6. Once again note the good agreement between measurements, tracking and theory. The use of the tune scan data thus allowed for much greater accuracy than if the island and core tune had been measured at only a single core tune, as is the case for the readback later described in Section 5.2.5.

5.2.3 Measuring the Island Orbit Phase Advance

Estimating the angle χ relating to the island orbit phase advance is relatively simple. From Eq. (3.27), we have

$$\chi = 2n\pi - 3\tilde{\phi}_{\mathrm{SFP}}, \tag{5.8}$$

where the islands are indexed $n = -1$, 0, or 1. Assume we have a set of measurements $\tilde{\phi}_{SFP,n}^{(i)}$ with standard uncertainties $\sigma_{\phi,n}^{(i)}$, where n indicates the island orbit in question and i is the measurement index. A chi-squared fit of χ

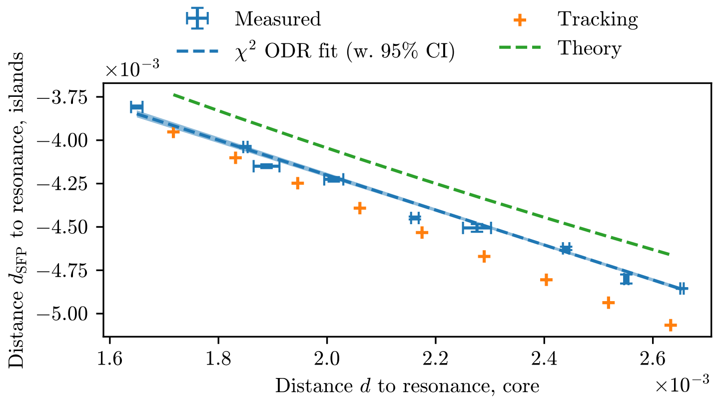

Figure 5.6: The measured island tunes as a function of the core tune, compared to both tracking and theory.

is then given by

$$\hat{\chi} = \underset{\chi}{\operatorname{argmin}} \sum_{n,i} \left(\frac{\chi - (2n\pi - 3\tilde{\phi}^{(i)}_{SFP,n})}{\sigma^{(i)}_{\phi,n}} \right)^2 . \tag{5.9}$$

Note that $\tilde{\chi}$ depends on the choice of interval used to represent $\tilde{\phi}_x$. The interval $[\phi_0, \phi_0 + 2\pi)$ should be chosen such that, for each n, no two $\tilde{\phi}^{(i)}_{SFP,n}$ are separated by the discontinuity at ϕ_0. Figure 5.7 shows a fit of χ, compared to tracking and theory. It was found that χ does not vary significantly over a tune scan, so measurements $\tilde{\phi}^{(i)}_{SFP,n}$ from different tunes were combined into a single estimate using Eq. (5.9).

5.2.4 Evaluation of TRIBs Parameter Measurements

As will be discussed in Section 6, a TRIBs optics ID correction scheme has been developed. Before evaluating this correction scheme, the uncorrected optics are used to evaluate the performance of the TRIBs parameter estimations outlined in Sections 5.2.1 to 5.2.3. These measurements are taken at different FinEstBeAMS ID gaps, comparing the measured TRIBs parameters with the predicted parameters of the AT lattice. The TRIBs optics at open gaps will be called the *reference condition*. For now, the dependence of the parameters on ID gap will be left implicit, as this will later be analyzed in Section 6. For as accurate measurements as possible, a low beam current of 3 mA was used. This current is low enough that all of the current can be driven to the islands at the same time without triggering safety interlocks, thus allowing separate measurements of the core and island orbit. A detailed description of the tune scan procedure can be found in Appendix C.

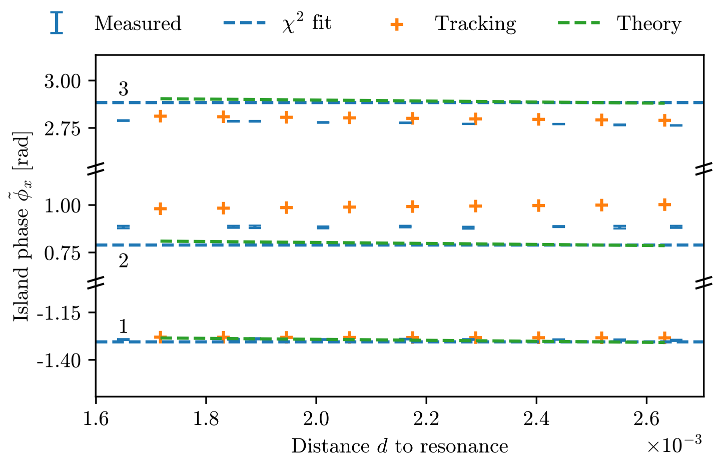

Figure 5.7: The measured values of the island phase $\tilde{\phi}_{\mathrm{SFP}}$ over a tune scan compared to the chi-squared fit of χ, tracking and theory. The island numbering is consistent throughout relevant figures.

Figure 5.8 shows such a comparison between α and $|F|$ as measured using the the tune scan and island tune techniques. The results are compared to the theoretical predictions based on the AT lattice. The figure shows that the island tune technique is far more reliable, showing a drastically lower variance between measurements. The systematic differences between the predicted and measured values of the TRIBs parameters will be further discussed in Section 6.

It should be noted that these measurements were taken on different beamtime shifts over the course of a few days. The exact conditions at each measurement can therefore vary due to, for example, thermal effects. In most cases, these differences in machine condition are significant enough to be measurable, and care should therefore be taken when comparing measurements taken at different times. In Fig. 5.8, the variance in the predicted parameters is dominated by the changes in ID gap, which can be seen by comparing with the uncertainties listed in Tab. 3.1.

In Fig. 5.9, the estimated value for χ is compared with the calculated values of the AT lattice. It was found that, in contrast to α and $|F|$, the value of χ was dominated by differences in machine condition and varied comparatively little with the ID gap. This is illustrated by the annotations in Fig. 5.9, which shows that the measured value of χ at the reference condition varies significantly between beamtime shifts. The predicted values also vary between each beamtime shift, due to the difference between LOCO measurements.

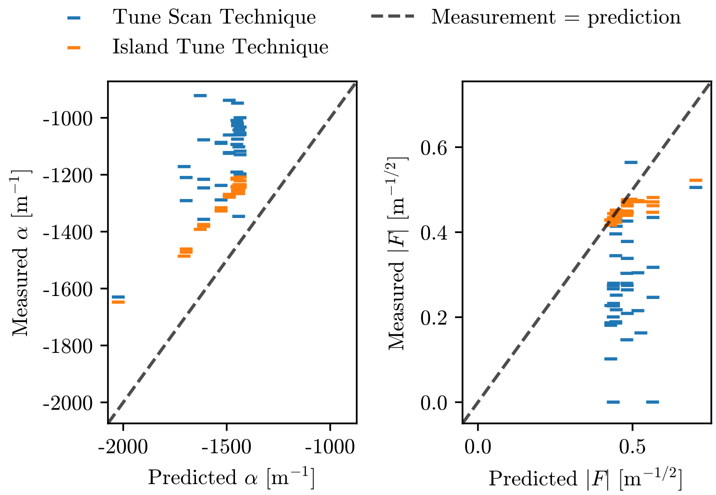

Figure 5.8: A comparison between the tune scan and island tune techniques used to measure the TRIBs parameters α and $|F|$, plotted versus the predicted parameters of the AT lattice.

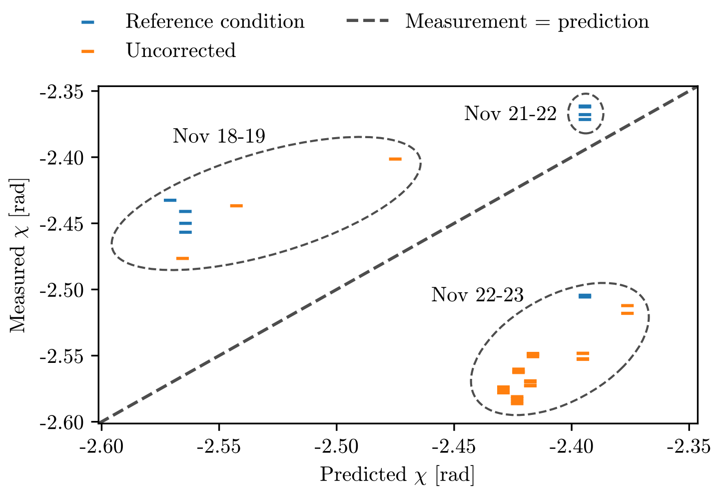

Figure 5.9: A comparison between the measured χ at the reference condition and uncorrected optics at different ID gaps plotted versus the theoretical prediction. The clusters are annotated by measurement date, clearly demonstrating the effect of machine condition.

5.2.5 Online Readback of the TRIBs Parameters

The island tune technique from Section 5.2.2 and TRIBs orbit phase advance measurement from Section 5.2.3 can be used to create an online readback of the TRIBs parameters. By continuously monitoring the island and core tune readback, as well as the island positions measured using the diagnostic beamlines, the TRIBs parameters can be calculated and monitored with only a small impact on the beam due to the transverse excitation required for tune readback. One possible application of this kind of readback is in an ID compensation feedback, later discussed in Section 6.3.

Such a TRIBs parameter readback was tested in the current implementation of the TRIBs delivery mode. A total beam current of 200 mA was used in multibunch mode with an even fill pattern. One of the 32 bunches was driven to the islands, while the remaining current stayed in the core. The main challenge in the delivery mode, as compared with the measurements in Section 5.2.4, is that both the island and core orbits must be measured simultaneously.

The horizontal tunes of the island bunch and one of the core bunches were excited using the stripline kicker, with each bunch monitored by a separate BbB readback channel. The measurement of the island orbit position using the diagnostic beamlines was severely affected by the light from the core bunches. Since the total current in the core is almost two orders of magnitude greater than each of the three island buckets, glare and diffraction from the core orbit was enough to overpower the light from the islands. This affected beamline B especially, due to the smaller separation between the core and island orbits. As a result, only the island furthest from the core (island 2 as seen in Fig. 5.3) could be confidently identified and measured, as shown in Fig. 5.10. The horizontal position of this island was measured by subtracting a fit of the core light profile and only considering a small area of interest around the island position.

The tune spectra and images were acquired at a rate of roughly 1 Hz in order to have ample time for image processing. Using $\hat{d}$, $\hat{d}_{\mathrm{SFP}}$, $\hat{x}_{A,2}$ and $\hat{x}_{B,2}$, the island phase space position was calculated according to Eq. (5.1) and the TRIBs parameters according to Eqs. (5.6), (5.7) and (5.9). The resulting timeseries is shown in Fig. 5.11. The overall 1σ noise level of the raw readback was $\sigma_\alpha = 33\ \mathrm{m}^{-1}$, $\sigma_{|F|} = 0.014\ \mathrm{m}^{-1/2}$ and $\sigma_\chi = 0.0097$ rad. It should be noted that due to the low sampling frequency, only a subset of the tune readback and image samples was used. The performance of a proper readback device could therefore be improved by using all available measurement samples.

To give an idea of the performance achievable with some simple filtering, an exponential moving average (EMA) filter is used as an example in Fig. 5.11, where the estimate X_t of each parameter at the measurement time t is updated based on the previous estimate X_{t-1} according to $X_t = \alpha_f \hat{X}_t + (1 - \alpha_f)X_{t-1}$. The weight of the last measurement $0 < \alpha_f < 1$ can be decreased to decrease

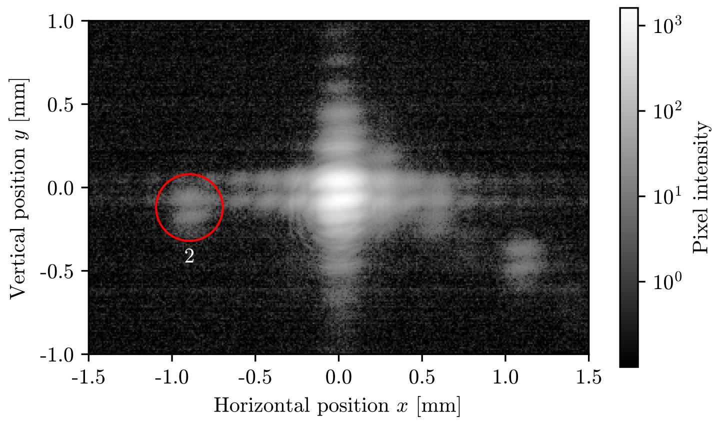

Figure 5.10: An image from diagnostic beamline B during the readback test, with pixel intensities shown in log scale. The red circle indicates the only island which could be confidently identified, as the other islands are likely covered by glare and diffraction patterns from the core orbit. The peak at $x = 1.0$ mm and $y = -0.5$ mm is not an island, and is likely a reflection from the core. The island numbering is consistent throughout relevant figures.

measurement noise at the cost of a slower response to fast changes.

5.3 Limitations of the Analytical Hamiltonian

The Hamiltonian as given by Eq. (3.24), has a three-fold radial symmetry which means that the three island orbits all have the same action J_{SFP} with a relative phase advance of exactly $2\pi/3$ between each island. As previously shown in Fig. 4.2, this symmetry does not hold in tracking, demonstrating that the stable fixed points of the AT lattice are neither all at the same action nor at phases $2\pi/3$ apart. Similar differences between the island orbits can also be seen in measurements, as shown by the consistent differences between island actions seen in Fig. 5.5 and island phase advances seen in Fig. 5.7. The effect is also visible in the phase space reconstruction in Fig. 5.4.

These slight differences in island positions can also be observed using the *beam position monitors* (BPMs). While the BPMs are not designed to measure the positions of multiple orbits at the same time it is assumed that, to first order, the BPMs can still be used to measure the center of charge given by

$$\bar{u} = \sum_n w_n u_n \tag{5.10}$$

where we sum over each orbit n with a fraction w_n of the total beam current and the position u_n. The BPM measurements thus give very little information about the positions of the individual islands.

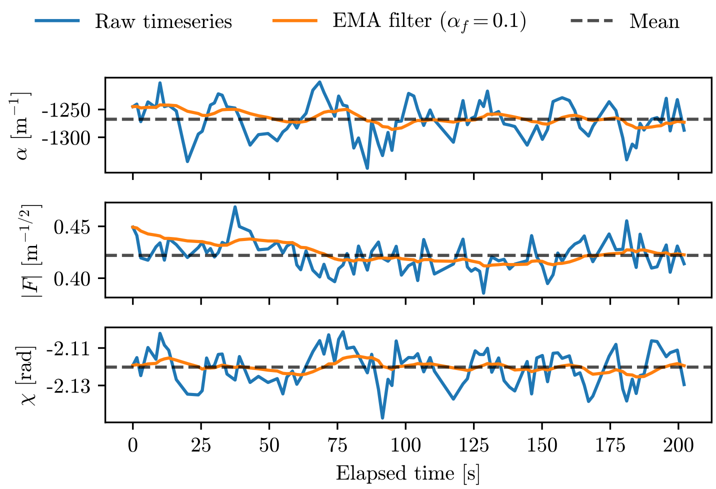

Figure 5.11: A timeseries of the measured TRIBs parameters during the read-back test. As an example, the raw timeseries is compared to an EMA filter.

In the case of evenly populated islands, the center of charge coincides with the average position of the three islands. Using the definition of the action-angle coordinates in Eq. (2.16), it can be shown that the stable fixed points in Eq. 3.27 result in a mean island position

$$\bar{x} = x_1 + x_2 + x_3 = \sum_{n=1}^{3} \sqrt{2\beta_x J_{\mathrm{SFP}}} \cos \frac{2n\pi - \chi}{3} = 0, \tag{5.11}$$

at all positions along the ring. This is not the case if the islands differ in action and relative phase advance, and as seen in Fig. 5.12, the BPMs measure a non-zero mean island position. Additionally, the effect of cross-plane coupling between the horizontal and vertical planes is clearly visible in the vertical island positions.

These differences between the islands are a clear indication of the impact of additional phase-dependent driving terms on the non-linear dynamics that are not included in the resonant Hamiltonian. This is to be expected, given that only a select few driving terms are included Eq. (3.24). While it has been shown that the Hamiltonian captures the overall behavior of the three islands well, the BPM measurements in Fig. 5.12 is a clear example of where the limitations of this relatively simple model can lead to incorrect conclusions.

5.4 Single Island Measurements

Imaging using diagnostic beamlines has been proven to be a reliable method of measuring the transverse position of the island orbits, but the technique has a

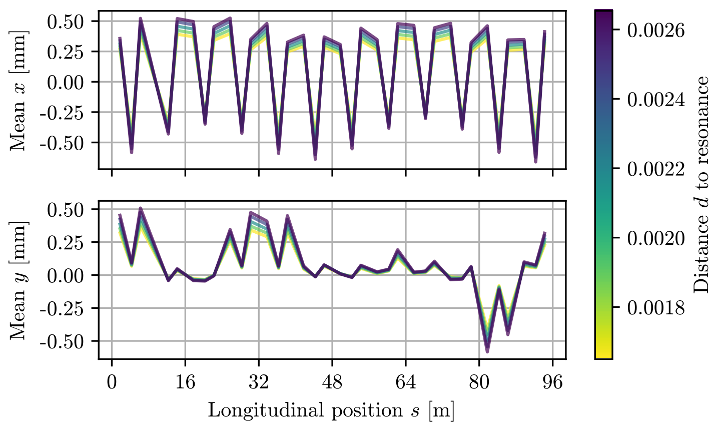

Figure 5.12: The mean island positions, in relation to the core orbit, as measured during a tune scan by the BPMs along the ring.

number of limitations. The beam can only be imaged at the two source positions, and the exact coordinates s_A and s_B are relatively uncertain. In addition, processing the images is computationally expensive. A promising alternative to imaging is to use the Turn-by-Turn (TbT) capabilities of the BPMs or use the BbB device. As opposed to imaging, these devices are not capable of resolving multiple orbits at the same time. A way of getting around this limitation is to only populate one of the island buckets. Since the TRIBs orbit passes three times through each s_0 before forming a closed loop, the bunch would appear to alternate between the three different stable fixed points at s_0. Thus, all three stable fixed points can be measured. The measurements in this section are done in single bunch mode, as the clear distinction between each turn simplifies data analysis.

5.4.1 Measurement and Optimization of Island Populations

It is first necessary to be able to measure the relative island populations. For this purpose, an optical beam splitter was used to redirect a portion of the light from diagnostic beamline A onto a photodiode. Due to the large separation between the islands at s_A, it was then possible to physically block out the light from the core and two of the islands. Thus only the synchrotron light from one of the island orbits could reach the photodiode. By monitoring the signal using an oscilloscope, as seen in Fig. 5.13, the relative light intensities of the different islands could be measured. The relative population of the islands is estimated using the integrated signal intensity of each peak. The core population could be approximated using the images from the diagnostic beamlines by comparing the integrated pixel intensity of the core orbit relative to the three island orbits.

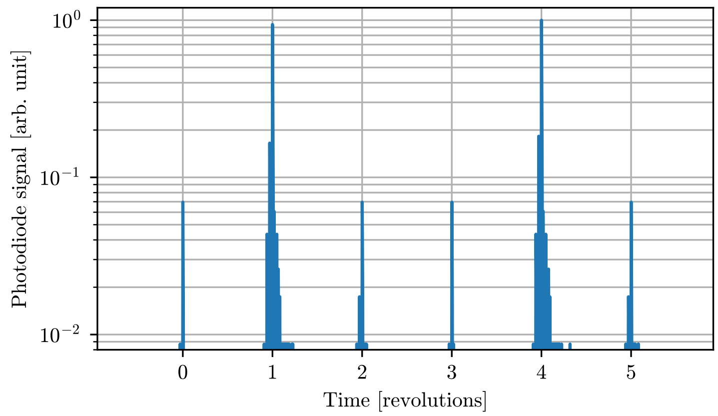

Figure 5.13: The photodiode signal amplitude over time expressed in units of revolution time. The majority of the current is contained in one of the island buckets, leading to a large signal every three turns. Note that the current was spread over a small bunch train, slightly widening each peak.

A method for preferentially populating one of the islands was found empirically by alternating between transversely exciting the horizontal core or island tune. A transverse excitation was applied by the stripline kicker at the core tune for two out of every three turns, driving the bunch current towards the islands. On the remaining turn, an excitation was applied at the island tune driving some of the current back towards the core orbit. Over the course of a few seconds, this resulted in a population equilibrium between the core and each of the three islands.

Crucially, the equilibrium populations between different islands was found to differ significantly. These transverse excitations are applied as a frequency sweep. By adjusting the parameters of both excitations (sweep center frequency, frequency range and period), the equilibrium orbit populations could be optimized empirically. The optimal parameters varied depending on the horizontal tune and ID gaps, and thus needed to be adjusted for each condition.

5.4.2 Correcting for Island Populations

While a very high single island population could sometimes be achieved, this was not always the case. It is therefore of interest to correct for residual current in the remaining island buckets. Suppose a core population w_0 and island bucket populations w_1, w_2, w_3 given in chronological order of when each island population is measured by the photodiode. Given TbT measurements $\bar{x}_{m,1}$, $\bar{x}_{m,2}$ and $\bar{x}_{m,3}$ of the islands, also ordered in chronological order, the center-of-charge assumption in Eq. (5.10) can be used to show that the measured positions are given by

$$\begin{bmatrix} \bar{x}_{m,1} \\ \bar{x}_{m,2} \\ \bar{x}_{m,3} \end{bmatrix} = \begin{bmatrix} w_0 & w_1 & w_2 & w_3 \\ w_0 & w_2 & w_3 & w_1 \\ w_0 & w_3 & w_1 & w_2 \end{bmatrix} \begin{bmatrix} \bar{x}_0 \\ \bar{x}_1 \\ \bar{x}_2 \\ \bar{x}_3 \end{bmatrix}. \tag{5.12}$$

where both the measurements $\bar{x}_{m,1}$ and the actual orbit positions $\bar{x}_m$ are given in a coordinate system relative to the BPM. Now consider a coordinate system relative to the core orbit such that $x_0 = 0$ and $x_n = \bar{x}_n - \bar{x}_0$. Also express the measured positions as $x_{m,n} = \bar{x}_{m,n} - \bar{x}_{m,0}$ where $\bar{x}_{m,0}$ is a reference measurement of the core position without any islands present. Assuming $x_{m,0} = \bar{x}_0$, this change of coordinate systems yields

$$\begin{bmatrix} x_{m,1} \\ x_{m,2} \\ x_{m,3} \end{bmatrix} = \begin{bmatrix} w_1 & w_2 & w_3 \\ w_2 & w_1 & w_2 \\ w_3 & w_3 & w_1 \end{bmatrix} \begin{bmatrix} x_1 \\ x_2 \\ x_3 \end{bmatrix}. \tag{5.13}$$

Note that Eq. (5.13) implicitly takes the core population w_0 into account since $w_0 = 1 - w_1 - w_2 - w_3$. Let the matrix in Eq. (5.13) be $\mathbf{W}$. This matrix is invertible if the determinant of $\mathbf{W}$ is non-zero

$$\begin{aligned} \det(\mathbf{W}) &= 3w_1w_2w_3 - w_1^3 - w_2^3 - w_3^3 \\ &= -\frac{1}{2}(1 - w_0)\big((w_1 - w_2)^2 + (w_2 - w_3)^2 + (w_3 - w_1)^2\big) \neq 0, \end{aligned} \tag{5.14}$$

It follows that $\mathbf{W}$ is invertible as long as there is current in the island orbits and the populations of all islands are not all identical. Thus, for an uneven island population, the estimated island orbit positions $\hat{x}_n$ are given by

$$\begin{bmatrix} \hat{x}_1 \\ \hat{x}_2 \\ \hat{x}_3 \end{bmatrix} = \hat{\mathbf{W}}^{-1} \begin{bmatrix} x_{m,1} \\ x_{m,2} \\ x_{m,3} \end{bmatrix}. \tag{5.15}$$

5.4.3 Turn-by-turn BPM Measurements

Using the island population estimates described in Section 5.4.1 together with Eq. (5.15), a test of the BPM TbT measurements was carried out. Two series of measurements were taken one after the other with the same core tune and sextupole configuration during the same shift, which should guarantee near-identical conditions. The islands were unevenly populated, reaching estimated island populations of $\hat{w}_1 = 88.6\% \pm 0.7\%$, $\hat{w}_2 = 6.3\% \pm 0.7\%$ and $\hat{w}_3 = 5.1\% \pm 0.5\%$ for both measurement series. No core population w_0 could be observed using the diagnostic beamlines. Each measurement recorded TbT data from all BPMs over a total of 20480 turns.

In Fig. 5.14, the estimated island positions from these two measurement series are shown. The plotted uncertainty takes into account the uncertainty in

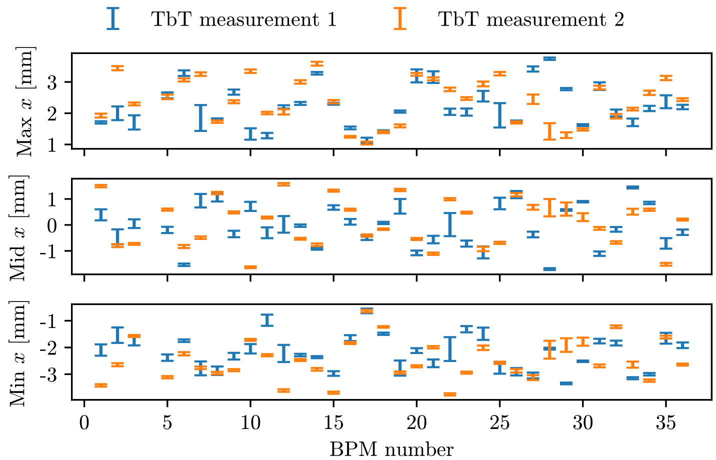

Figure 5.14: A comparison between the two TbT measurement series taken at near-identical conditions, illustrating significant disagreement. The plot is divided into $\hat{x}_{min} < \hat{x}_{mid} < \hat{x}_{max}$ for legibility.

$\hat{w}_1$, $\hat{w}_2$, $\hat{w}_3$ through Monte-Carlo estimation. This figure illustrates significant disagreement between the two measurements, which is not well-explained by measurement noise. To compare the TbT measurements with those done using the diagnostic beamlines, both position estimates are plotted against tracking in Fig. 5.15. As the plot shows, the agreement between the TbT measurements and tracking is poor, while the diagnostic beamline measurements agrees well with tracking.

5.4.4 Bunch-by-Bunch Measurements

During the same test as the TbT data, the BbB device was also used to make measurements. The BbB device does not have an absolute calibration, meaning that the island positions are measured in arbitrary units. To be able to compare these measurements with tracking, the three island positions are normalized to unit variance $\hat{x}_i/\sigma_x$, where $\sigma_x^2 = \sum_i (\hat{x}_i - \langle \hat{x} \rangle)^2$. These measurements are shown in Fig. 5.16, where the diagnostic beamline measurements have been added for comparison.

In contrast to the TbT measurements, the BbB measurements were repeatable, and show good agreement with tracking. This difference is somewhat surprising since the BPMs and BbB device use identical hardware mounted in the ring, consisting of four pick-up electrodes inside the vacuum chamber. There are, however, a few key differences in the processing of the pick-up signals. Firstly, the BbB device uses analogue hardware to combine the signal from the pick-ups, before using an *analogue-to-digital converter* (ADC) to digitize the reading,

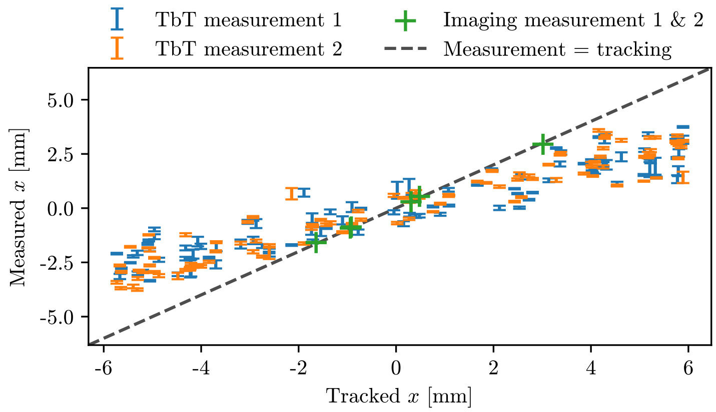

Figure 5.15: A comparison of the agreement with tracking for the two TbT measurement series and imaging using the diagnostic beamlines.

while the BPMs use ADCs to digitize the signals before being combined digitally. Secondly, the BPMs use what is called *condition switching*, which corrects for the relative sensitivity of the pick-ups with respect to the absolute beam position. The condition switching must be turned off during the TbT measurements. It is suspected that the poor repeatability of the TbT measurements is caused by the BPMs retaining their previous state from when the condition switching was turned off, but this has not been verified.

Since the BbB measurements are not currently calibrated, the island action J_{SFP} could not be estimated. However, the normalized island positions $\hat{x}/\sigma_x$ gives some information about the phase advance of the islands, which could be used as an additional method to estimate χ. There is also potential for improvement, since the BbB device can in principle be calibrated as long as the individual bunch current is taken into account.

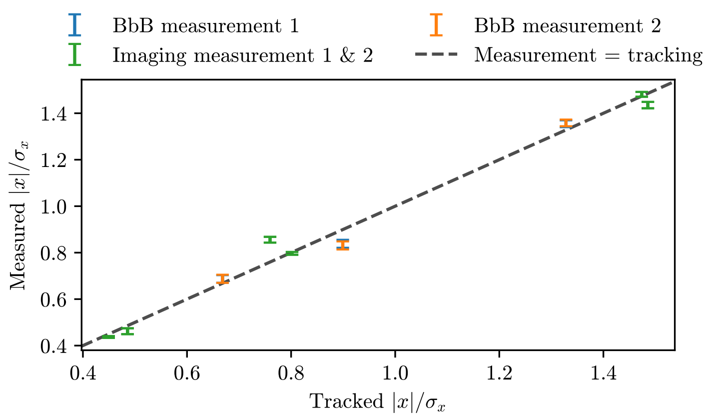

Figure 5.16: A comparison of the agreement with tracking between the two BbB measurements and imaging using the diagnostic beamlines. Note that the two BbB measurements may be hard to distinguish due to overlap. Since the BbB measurements are not calibrated, the relative positions of the islands are normalized to unit variance. The absolute value $|\hat{x}|/\sigma_x$ is used for legibility only.

6 Compensation of Insertion Devices

As detailed in Section 4.2.2, the effect of the IDs can be modeled by a combined quadrupole and octupole field. These fields perturb the TRIBs orbit in three main ways, namely

- tune shifts due to the quadrupole field,
- beta-beating due to the quadrupole field, and
- a first-order change in the ADTS due to the octupole field.

Of these, only the tune shift is currently compensated using the tune feedback device. This ensures d can be kept constant, neglecting transient behavior when gaps are adjusted. The beta-beating gives rise to a change in the TRIBs parameters α and F due to the dependence on β_x in Eq. (3.5), while the octupole component results in a change of α since $\Gamma_{2200}(s) \propto k_3(s)$.

To compensate for the effects of the IDs on the TRIBs optics, a compensation scheme has been developed to restore the open-gap values of the TRIBs parameters by adjusting the sextupole families SDo, SDi and SCi. To first order, this should keep the position of the island orbits constant while also preserving additional features of the non-linear optics such as the island tunes and the island bucket area. In addition to restoring the TRIBs parameters, an additional constraint was imposed on the correction to adjust the sextupoles in such a way that the chromaticity in both planes stayed constant.

While the effect of the octupole field on α is straight forward to calculate based on the multipole expansion fit of the ID kickmaps, the effect of the beta-beating is not as trivial. While this can conceivably be calculated perturbatively, it is more practical to directly calculate the TRIBs parameters of the AT lattice after inserting the ID multipole expansion and adjusting the tune as described in Section 4.2.3. This effectively means that the beta-beating caused by the IDs is not measured, but instead approximated using AT.

6.1 Correcting the TRIBs Parameters

To regain the open-gap parameters α_0, F_0, ξ_{x0} and ξ_{y0} for a lattice with closed gaps, the sextupole strengths must be optimized numerically. The optimization is based on the formulation of the TRIBs parameters given in Section 3.2.4.

Consider a family or sub-family of sextupoles that share a power-supply. Define the set $S = \{u_1, u_2, \cdots u_n\}$ consisting of all the sextupoles in this grouping, with the common sextupole strength $k_2^{(u)} = k_S$ for all $u \in S$. The derivatives of the TRIBs parameters with respect to k_S are given by summing each contribution in Eq. (3.44) according to

$$\begin{aligned}
\frac{\partial \alpha}{\partial k_S} &= \sum_{u\in S}\sum_{v}\left(\mathcal{G}_{\alpha}^{(uv)}+\mathcal{G}_{\alpha}^{(vu)}\right)k_2^{(v)}, & \frac{\partial \xi_x}{\partial k_S} &= \sum_{u\in S}\mathcal{G}_{\xi x}^{(u)},\\
\frac{\partial F}{\partial k_S} &= \sum_{u\in S}\mathcal{G}_{F}^{(u)}, & \frac{\partial \xi_y}{\partial k_S} &= \sum_{u\in S}\mathcal{G}_{\xi y}^{(u)}.
\end{aligned} \tag{6.1}$$

Let $S_1, S_2, \cdots S_{38}$ be the 38 groups of sextupoles consisting of the SDo and SDi families and the SCo and SCi sub-families. Further define the column vector $\mathbf{k}_2 = [k_{S_1}, k_{S_2}, \cdots, k_{S_{38}}]^\top$ consisting of the sextupole strengths of each group. The parameters of interest are gathered in the vector-valued real function $\mathbf{P}(\mathbf{k}_2) = [\alpha, \operatorname{Re} F, \operatorname{Im} F, \xi_x, \xi_y]^\top$, where the real and imaginary parts of F are separated for reasons that will soon become apparent. This function has the 5×38 Jacobian matrix

$$\mathbf{J_P}(\mathbf{k}_2) = \begin{bmatrix}
\frac{\partial\alpha}{\partial k_{S_1}} & \frac{\partial\alpha}{\partial k_{S_2}} & \cdots & \frac{\partial\alpha}{\partial k_{S_{38}}}\\
\operatorname{Re}\left[\frac{\partial F}{\partial k_{S_1}}\right] & \operatorname{Re}\left[\frac{\partial F}{\partial k_{S_2}}\right] & \cdots & \operatorname{Re}\left[\frac{\partial F}{\partial k_{S_{38}}}\right]\\
\operatorname{Im}\left[\frac{\partial F}{\partial k_{S_1}}\right] & \operatorname{Im}\left[\frac{\partial F}{\partial k_{S_2}}\right] & \cdots & \operatorname{Im}\left[\frac{\partial F}{\partial k_{S_{38}}}\right]\\
\frac{\partial\xi_x}{\partial k_{S_1}} & \frac{\partial\xi_x}{\partial k_{S_2}} & \cdots & \frac{\partial\xi_x}{\partial k_{S_{38}}}\\
\frac{\partial\xi_y}{\partial k_{S_1}} & \frac{\partial\xi_y}{\partial k_{S_2}} & \cdots & \frac{\partial\xi_y}{\partial k_{S_{38}}}
\end{bmatrix}, \tag{6.2}$$

where the dependence on $\mathbf{k}_2$ stems solely from the derivative of α in Eq. (3.44). For small changes $\Delta\mathbf{k}_2$, the change in the parameters $\Delta\mathbf{P}$ is therefore given by

$$\Delta\mathbf{P} \approx \mathbf{J_P}\Delta\mathbf{k}_2. \tag{6.3}$$

The AT lattice parameters can now be optimized to a set of desired parameters $\mathbf{P}_0$ using the Newton-Raphson method. This is achieved by iteratively solving Eq. (6.3) for a $\Delta\mathbf{k}_2$ such that $\mathbf{P}(\mathbf{k}_2) + \Delta\mathbf{P} = \mathbf{P}_0$. Formally, the optimization is given by iterating $\mathbf{k}_2^{old} \to \mathbf{k}_2^{new}$ using

$$\begin{aligned}
\mathbf{k}_2^{new} &= \mathbf{k}_2^{old} + \Delta\mathbf{k}_2,\\
\Delta\mathbf{k}_2 &= -\mathbf{J}_\mathbf{P}^{+}(\mathbf{k}_2^{old})\,\Delta\mathbf{P},\\
\Delta\mathbf{P} &= \mathbf{P}(\mathbf{k}_2^{old}) - \mathbf{P}_0,
\end{aligned} \tag{6.4}$$

until the errors $\Delta\mathbf{P}$ are below a desired threshold. Here, $\mathbf{J}_\mathbf{P}^{+}$ is a pseudoinverse of $\mathbf{J_P}$, which is required since Eq. 6.3 is underdetermined, meaning there are more sextupole groups than parameters we wish to optimize. The real and imaginary parts of F are separated since the pseudoinverse of a complex-valued matrix is not guaranteed to be real, which would result in complex valued corrections

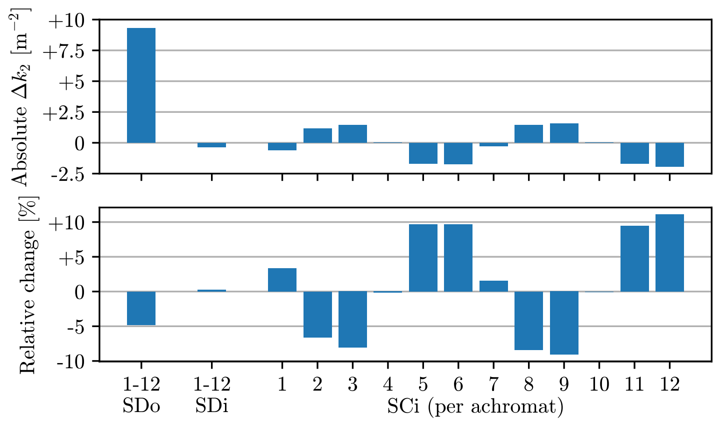

Figure 6.1: An example of the absolute and relative sextupole strength changes of the 14 magnet families and sub-families to compensate a gap of 20 mm in FinEstBeAMS.

$\Delta\mathbf{k}_2$. Here, the Moore-Penrose pseudoinverse is used, yielding the least-squares solution for $\Delta\mathbf{k}_2$ at each iteration [22]. It is desirable to use the the least squares solution for the sextupole corrections, since any change to the sextupole strengths will affect other aspects of the non-linear optics not considered here, which ultimately may have a negative impact on machine performance. Additionally, small corrections decrease the chance of saturating any of the sextupole power supplies.

The corrector magnets SDo, where each magnet is powered individually, are nominally not used at MAX IV. In addition, it was found that these magnets did not contribute meaningfully to the correction of the TRIBs parameters, and were therefore excluded from the optimization. This reduces the degrees of freedom by 24 without sacrificing performance, since the remaining 14 degrees of freedom still result in a multitude of solutions. An example of the sextupole corrections applied at a FinEstBeAMS ID gap of 20 mm is shown in Fig. 6.1.

6.2 Measurements of the TRIBs ID Compensation

The optimization of the TRIBs parameters outlined in Section 6.1 was used on the machine to compensate for the predicted effect of the ID on the TRIBs parameters. To eliminate additional sources of error, the optimization was done using a LOCO fit from the same measurement shift. Although the correction scheme is not limited to the compensation of a single ID, the measurements were limited to only the FinEstBeAMS ID to decrease the total number of measurements needed.

The effectiveness of the compensation scheme was evaluated using the island

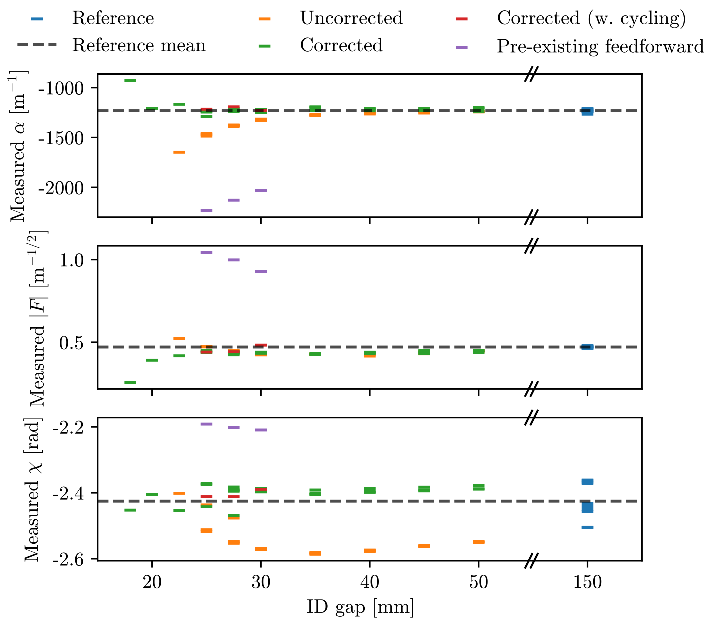

Figure 6.2: The measured TRIBs parameters at different ID gaps for the reference condition, without correction, with correction, correction with cycling and the pre-existing feedforward scheme.

tune technique outlined in Section 5.2.2 and the measurement of χ outlined in Section 5.2.3. The effect of closing the ID gap of FinEstBeAMS was measured, comparing results with and without correction at a large range of gaps. It should be noted that, as with the measurements of the uncorrected optics in Section 5.2.4, these measurements span several days which means that the machine condition may vary. A few additional small-scale tests were carried out over a smaller range of gaps. The first such test used the pre-existing feedforward device to correct the TRIBs optics to serve as a comparison. To provide a few baseline measurements free of hysteresis effects in the sextupole corrections, a second small-scale test was conducted where the sextupoles were cycled to the corrected settings.

An overview of this evaluation of the compensation scheme is shown in Fig. 6.2, showing the measured TRIBs parameters α, $|F|$ and χ for the corrected and uncorrected TRIBs optics over a range of ID gaps. It is clear that the parameters of the corrected optics are closer to the mean parameters of the reference condition than the uncorrected optics. The correction started to degrade for an ID gap of less than around 22.5 mm. There was no significant difference between the proposed compensation scheme with- or without cycling of the sextupoles, suggesting that the effects of hysteresis are negligible.

It should be noted that the measurements of the uncorrected TRIBs optics could only be done at ID gaps 22.5 mm and larger. As the ID approached the minimum possible gap of 14 mm, $|\alpha|$ increased while $|F|$ decreased. This decreases the action J_{SFP} of the island orbits, thus decreasing the separation of the core and island orbit. Qualitatively, it was observed that once the separation between island and core orbits became too small, the core and island buckets started to merge, and the motion became unstable. This made tune scans of the uncorrected optics too difficult for ID gaps lower than 22.5 mm.

The proposed compensation scheme increased the separation between the core and island, allowing for tune scans to be performed at ID gaps of 20 mm and 18 mm. The corrected optics instead failed at a ID gap of 17 mm, exhibiting a different mode of failure than the uncorrected optics. Instead of the island and core buckets merging, the amplitude of the island orbit increased at lower gaps. At 17 mm, the island orbit population was no longer stable, as the current in the island orbit would slowly (over the span of a few seconds) diffuse back into the core orbit. As a possible explanation for the different failure modes, it is noted that at lower ID gaps the uncorrected optics exhibit a large increase in the detuning $|\alpha|$, while the corrected optics show a decrease in the resonance strength $|F|$.

The chromaticity at each condition was also measured, with the results shown in Fig. 6.3. Similar to χ, there was significant variability in the measured chromaticity between measurements of the reference condition, making comparisons between the uncorrected and corrected optics difficult. Nevertheless, the horizontal and vertical chromaticity of both the uncorrected and corrected optics does not significantly differ from the reference condition.

6.2.1 Measured Versus Theoretical TRIBs Parameters

The error between the measured and theoretical TRIBs parameters α and $|F|$ is shown in Fig. 6.4. The error in χ is not included due to the large difference between measurement shifts, as seen in Fig. 5.7. As the plot shows, the measured resonance strength α consistently differs by around $\Delta\alpha \approx 200$ m^{-1}. The discrepancy appears to be relatively constant up to a gap of around 25 mm, and is the same for both the corrected and uncorrected optics.

The source of this offset is not fully understood. A possible explanation is the difference between the AT lattice and the machine. However, as shown in Fig. 4.2, the amplitude of the island orbit was generally larger in tracking than what was predicted by the analytical Hamiltonian, which corresponds to a similar increase in α. It is therefore suspected that part of this error is due to the simplifications and assumptions underlying the resonant Hamiltonian in Section 3.2. Much of the discrepancy could for example be explained by higher-order corrections to h_{2200}, the inclusion of additional detuning terms such as h_{3300}, cross-coupling between the planes, or a combination of several such

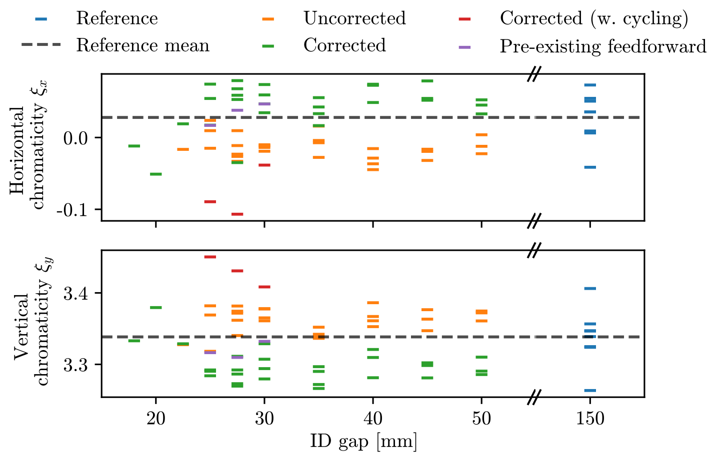

Figure 6.3: The measured chromaticity at different gaps for the reference condition, without correction, with correction, correction with cycling and the previous FF scheme.

effects. This is further supported by the many deviations from the three-fold symmetry of the resonant Hamiltonian seen in both tracking and measurements, as discussed in Section 5.3. It should be noted that it would be possible to include this $\Delta\alpha$ as an empirical correction factor when making predictions using analytical calculations on the 1.5 GeV ring, although the validity of such a correction should be carefully considered.

Furthermore, the systematic error between the measurements and theory does seem to increase at lower ID gaps. This discrepancy could be attributed to multiple potential factors. The first possible explanation is the relatively simple model used for the IDs. As is shown in Fig. 4.3, the effect of the kickmap is not fully captured by a combined quadrupole and octupole field, especially at large horizontal positions. Secondly, it is likely that the beta functions of the AT lattice are less accurate at lower ID gaps, since an open-gap LOCO measurement is used to extrapolate the effect of the ID quadrupole field and tune feedback. Both of these error sources could potentially be mitigated by using LOCO measurements done at lower ID gaps, which could be used to estimate both the quadrupole component of the ID field and the resulting beta functions. Additionally, the ID multipole fit could be adjusted by assigning greater weight to the residual fields at the predicted island positions. Although this approach could potentially lead to better agreement with measurements without including higher order multipoles, such a non-standard multipole expansion should also be considered carefully.

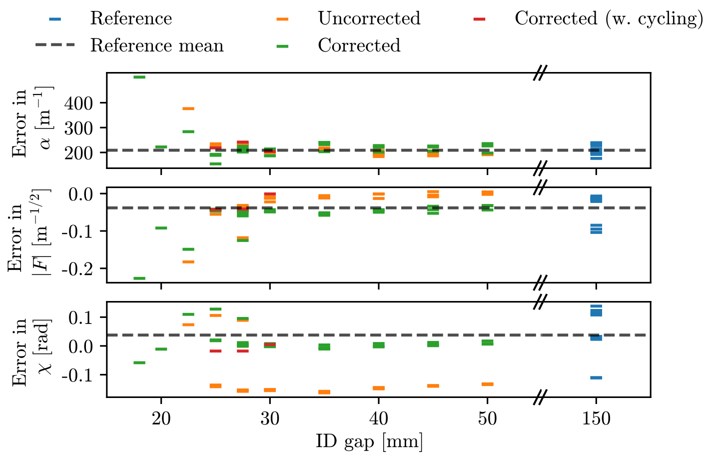

Figure 6.4: The difference between the measured and predicted TRIBs parameters as a function of ID gap for the reference condition, uncorrected optics, and corrected optics with and without cycling.

6.2.2 Lifetime

The beam lifetime is an important figure of merit which describes the rate of current loss in a storage ring. The instantaneous beam lifetime τ is given by

$$\frac{1}{\tau} = -\frac{\dot{I}}{I}, \tag{6.5}$$

where $\dot{I}$ is the current loss per unit of time. The lifetime is determined by multiple different sources of current loss, such as physical and aperture, momentum acceptance, scattering and the Touschek effect [23]. A high lifetime is desirable, as lower current loss means that top-up injections can be less frequent. A lower loss rate also represents a lower radiation exposure for the accelerator components.

The effect of the sextupole compensation scheme on beam lifetime was therefore quantified by measuring the lifetime of the TRIBs optics at a FinEstBeAMS ID gap of 25 mm in single-bunch mode with and without correction. The results are shown in Fig. 6.5, which demonstrates that the correction marginally increased the beam lifetime over all test conditions. The measurement could not be done for the island orbits at a bunch current of over 5 mA due to safety interlocks dumping the beam if the BPM readings are too far from the reference orbit. These measurements show that the ID compensation does not have a negative impact on the lifetime, suggesting that other aspects of the non-linear optics such as dynamic aperture and momentum acceptance is not degraded significantly by the sextupole corrections.

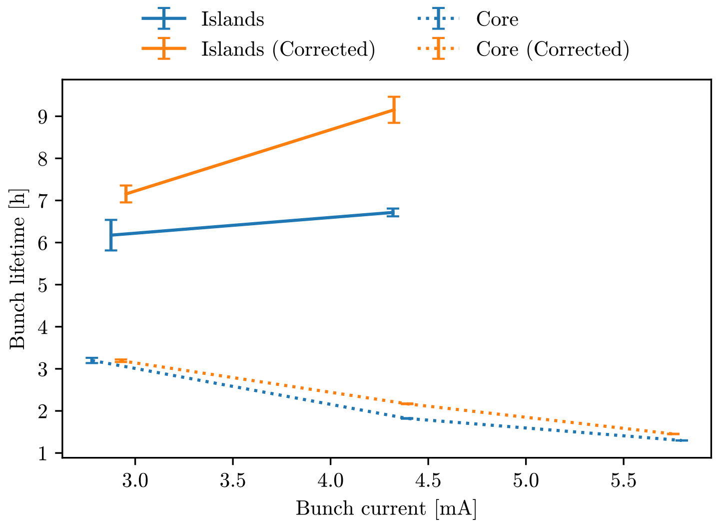

Figure 6.5: The single-bunch lifetime for the uncorrected and corrected for both island and core orbits.

6.3 Future Implementation

The final implementation of the ID compensation scheme is not within the scope of this thesis, but a few possible solutions will be discussed. The main approaches considered are either feedforward or feedback control. These approaches could also be applied simultaneously, where a feedforward ID compensation is combined with additional corrections applied by a feedback. The measurements in Section 6.2 were carried out similarly to a feedforward approach, where corrections are applied solely based on the predictions from the AT lattice without taking into account the measured TRIBs parameters in any way. The main benefit of a feedforward approach would be robustness, since no measurement noise (other than the initial LOCO measurements) can affect the correction. A feedforward device is also easy to implement and reacts quickly, as pre-calculated corrections can be stored in a *feedforward table* and applied as soon as an ID gap is moved. Pure feedforward devices are, however, sensitive to model errors (as can be seen at lower gaps in Section 6.2) due to the lack of a feedback mechanism. Additionally, unless an effective method is found to superimpose the corrections from multiple IDs, the size of the feedforward tables scale exponentially with the number of IDs considered, which may become an issue if more IDs than FinEstBeAMS and Bloch are to be included.

Instead, a feedback approach could be used to correct for a measured deviation $\Delta\hat{\mathbf{P}}$ from the desired TRIBs parameters. As demonstrated in Section 5.2.5, the tune readback and diagnostic beamlines could be used in delivery conditions to continuously measure the TRIBs parameters α, F and χ. The observed differences $\Delta\hat{\alpha}$, $\Delta|\hat{F}|$, $\Delta\hat{\chi}$ between the measured and desired TRIBs parameters could then be used to apply corrections. While there exists less invasive methods to measure the chromaticities [24, 25], which could be used to monitor $\Delta\hat{\xi}_x$ and $\Delta\hat{\xi}_y$ during operation, they have not yet been implemented at MAX IV. As the development of a chromaticity monitor would require a substantial development effort, the feedback could alternatively be designed to not affect the chromaticities by defining $\Delta\xi_x = \Delta\xi_y = 0$ as constants. Such a feedback must be carefully implemented, as model error can otherwise result in the chromaticities drifting over time.

For example, a simple proportional feedback could be implemented similarly to Eq. (6.4), where a sextupole correction $\Delta\mathbf{k}_2$ can be applied according to

$$\Delta\mathbf{k}_2 = -K_p \mathbf{J}_{\mathbf{P}}^{+}(\mathbf{k}_2^{old})\,\Delta\hat{\mathbf{P}}, \tag{6.6}$$

where the proportional gain $0 < K_p \leq 1$ is used to adjust the sensitivity of the feedback. In contrast to feedforward control, feedback control has the advantage of being less prone to model errors. However, it takes time for the feedback to react to changes, and the presence of measurement noise in $\Delta\mathbf{P}$ can make it less robust. Although this can be somewhat mitigated with filtering, this inherently results in a trade-off of slower response times as exemplified with the EMA described in Section 5.2.5.

7 Conclusions and Outlook

The theoretical framework of TRIBs parameters based on the resonant Hamiltonian as described in Section 3.2 has been evaluated quantitatively. The predictions of this framework, applied to the AT lattice of the 1.5 GeV ring, has been compared to both measurements and tracking. The two diagnostic beamlines have been used to reliably reconstruct the phase space position of the island orbit relative to the core, and TbT and BbB measurements of near single-island conditions have also been evaluated. While the TbT measurements do not seem to yield reliable results, the BbB measurements have been shown to be repeatable to a similar degree as the diagnostic beamline measurements. However, the current lack of absolute calibration of the BbB device means the measurements have limited utility.

To further compare the measurements to theoretical predictions, different experimental methods for estimating the TRIBs parameters α, $|F|$ and χ have been described and tested. The detuning parameter α and resonance strength $|F|$ have been estimated using two different methods, here named the tune scan and island tune techniques. Of these, the island tune technique was shown to be more reliable, yielding more repeatable and precise measurements of the two parameters. The island phase χ could also be reliably measured using the diagnostic beamlines.

The measured TRIBs optics broadly agree with theoretical calculations and tracking, with the notable exception of the measured detuning parameter α, which differs significantly from theory. The reason for this discrepancy is not known, but part of it could potentially be explained by higher-order terms neglected in the Hamiltonian. The theoretical framework nevertheless serves as a useful approximation which can be used for systematic studies of the TRIBs optics. A readback for online measurement of the TRIBs parameters based on the island tune technique has also been tested, which achieved a promising level of accuracy even at conditions similar to the proposed TRIBs delivery mode.

Using the theoretical framework, an ID compensation scheme for correction of the TRIBs parameters was developed. The compensation was tested on the machine using precalculated corrections, similar to feedforward control. Initial results are promising, as measurements show the TRIBs parameters could be successfully corrected down to a FinEstBeAMS gap of around 25 mm. Further research is required to determine if the performance of the ID compensation can be improved at lower ID gaps. As discrepancies between model and measurements increase, the performance of any feedforward correction worsens. It is therefore argued that the decreased performance of the feedforward at these gaps is not due to fundamental limitations of the sextupole correction scheme itself, and instead due to increased mismatch between the AT model and the machine at lower gaps. Possible sources of this mismatch include the multipole fits of ID kickmaps and the extrapolation of the closed-gap beta functions from open-gap LOCO measurements. Further research could also be directed towards the effects and compensation of skew multipole components in non-planar ID modes.

The implementation of a working ID compensation is yet to be done. Results show that a feedforward device based on the sextupole correction developed in this thesis would decrease the sensitivity of the TRIBs optics to ID gaps, although the performance at lower ID gaps still has potential for improvement. This likely hinges on a better understanding of the increased model mismatch at lower gaps, where further studies are needed. A feedback approach to ID compensation is also conceivable, where the island tune technique is used in combination with the diagnostic beamlines to continuously monitor the TRIBs parameters. Such a feedback could be implemented either as a standalone ID compensation, or acting in unison with a feedforward. Either way, further studies are needed to develop and test an online TRIBs parameter measurement and ID compensation feedback.

Acknowledgments

I would like to thank my supervisors Francis Cullinan and David K Olsson for their encouragement and support, especially during many long and late beamtime shifts. I would also like to thank Magnus Sjöström, Jonas Breunlin and Robin Svärd for offering their technical expertise on the MAX IV facility, the MAX IV operations team for their technical support during beamtime shifts, and Paul Goslawski and Michael Arlandoo at BESSY II for gladly sharing their experience and theoretical knowledge of TRIBs.

References

[1] I. Abrikosov *et al.*, "MAX IV conceptual design report," technical report, MAX IV Laboratory, Lund, Sweden, 2006.

[2] "Detailed design report," technical report, MAX IV Laboratory, Lund, Sweden, 2010.

[3] D. K. Olsson and Å. Andersson, "Studies on transverse resonance island buckets in third and fourth generation synchrotron light sources," *Nuclear Instruments and Methods in Physics Research Section A: Accelerators, Spectrometers, Detectors and Associated Equipment*, vol. 1017, p. 165802, 2021.

[4] M. E. Arlandoo, *Transverse Resonance Island Buckets in Advanced Light Sources*. Phd thesis, Humboldt-Universität zu Berlin, 2024.

[5] K. M. Nam, J.-G. Hwang, Y. D. Yoon, and Y. W. Parc, "Revised hamiltonian near third-integer resonance and implications for an electron storage ring," *Phys. Rev. Accel. Beams*, vol. 27, p. 044001, Apr 2024.

[6] F. Cullinan, Å. Andersson, A. Johansson, M. Sjöström, and P. F. Tavares, "TRIBs user test week on the MAX IV 1.5 GeV ring," Internal note 20250408, MAX IV Laboratory, 2025.

[7] S. Y. Lee, *Accelerator Physics*. World Scientific, 4th ed., 2018. Relevant pages: 34–56, 122–131, 159–162, 186–192 and 879–888.

[8] H. Wiedemann, *Particle Accelerator Physics*. Graduate Texts in Physics, Cham, Switzerland: Springer Cham, 4th ed., 2015. Relevant pages: 88–93, 315–321 and 539–556.

[9] A. Franchi, L. Farvacque, F. Ewald, G. Le Bec, and K. B. Scheidt, "First simultaneous measurement of sextupolar and octupolar resonance driving terms in a circular accelerator from turn-by-turn beam position monitor data," *Phys. Rev. ST Accel. Beams*, vol. 17, p. 074001, Jul 2014.

[10] C. Schmitz-Antoniak, "X-ray absorption spectroscopy on magnetic nanoscale systems for modern applications," *Reports on Progress in Physics*, vol. 78, p. 062501, 2015.

[11] C. Takahashi *et al.*, "Multi-dimensional feedforward controller at max iv," in *Proceedings of the International Beam Instrumentation Conference, IBIC*, pp. 335–338, JACoW Publishing, Geneva, Switzerland, 2022.

[12] W. Rogers, N. Carmignani, L. Farvacque, and B. Nash, "pyAT: A Python Build of Accelerator Toolbox," in *Proc. of International Particle Accelerator Conference (IPAC'17), Copenhagen, Denmark*, no. 8 in International Particle Accelerator Conference, (Geneva, Switzerland), pp. 3855–3857, JACoW, May 2017.

[13] A. Terebilo, "Accelerator toolbox for MATLAB," in *Workshop on Performance Issues at Synchrotron Light Sources*, 2001.

[14] S. Leemann, "Updates to the MAX IV 1.5 GeV storage ring lattice," Internal note 20120904, MAX IV Laboratory, 2012.

[15] J. Safranek, G. Portmann, A. Terebilo, and C. Steier, "MATLAB-based LOCO," in *Proceedings of EPAC 2002*, (Paris, France), pp. 1184–1186, 2002.

[16] V. Pricop, *Hysteresis effects in the cores of particle accelerator magnets.* Phd thesis, Transilvania University, Brasov, 2016.

[17] S. Leemann and H. Tarawneh, "Impact of insertion devices on the max iv storage rings," in *Proceedings of IPAC'15*, pp. 1696–1698, IPAC 2015, 2015.

[18] O. Chubar, P. Elleaume, and J. Chavanne, "A three-dimensional magnetostatics computer code for insertion devices," *Journal of Synchrotron Radiation*, vol. 5, pp. 481–484, May 1998.

[19] R. Tomás, M. Bai, R. Calaga, W. Fischer, A. Franchi, and G. Rumolo, "Measurement of global and local resonance terms," *Phys. Rev. ST Accel. Beams*, vol. 8, p. 024001, Feb 2005.

[20] M. Hofer and R. Tomás, "Impact of two-dimensional decoherence on the measurement of resonance driving terms," *Journal of Physics: Conference Series*, vol. 2687, p. 062006, Jan 2024.

[21] P. Virtanen *et al.*, "SciPy 1.0: Fundamental Algorithms for Scientific Computing in Python," *Nature Methods*, vol. 17, pp. 261–272, 2020.

[22] J. Stoer and R. Bulirsch, *Introduction to Numerical Analysis.* New York: Springer, 3rd ed., 2002. Relevant pages: 243–247.

[23] A. Rosborg, *Electron Beam Sizes and Lifetimes at MAX II and MAX III.* Phd thesis, Lund University, 2012.

[24] D. Cocq, O. R. Jones, and H. Schmickler, “The measurement of chromaticity via a head - tail phase shift,” *AIP Conf. Proc.*, vol. 451, no. 1, pp. 281–288, 1998.

[25] P. Zisopoulos and Y. Papaphilippou, “Extracting chromatic properties of electron beams from spectral analysis of turn-by-turn beam position data,” 2020. arXiv:1234.56789.

Appendix A: Detailed Second-order Calculations

To motivate the selection rules in Eq. 3.13, the *Poisson bracket* from classical Hamiltonian dynamics are introduced

$$\{f,\, g\} = \sum_{i=1}^{n} \frac{\partial f}{\partial q_i}\frac{\partial g}{\partial p_i} - \frac{\partial f}{\partial p_i}\frac{\partial g}{\partial q_i} \tag{A.1}$$

where f and g are functions dependent on the generalized coordinates $q_1, q_2, \cdots q_n$ and their respective conjugate momenta $p_1, p_2, \cdots p_n$ [4]. Using the definition of the basis functions in Eq. (3.1), it can be shown that

$$\begin{aligned}\{\, |jklm\rangle\,,\, |pqrt\rangle\,\} = \;& 2i(jq-kp)\,|j{+}p{-}1,\, k{+}q{-}1,\, l{+}r,\quad m{+}t\quad\rangle \\ &+2i(lt-mr)\,|j{+}p,\quad k{+}q,\quad l{+}r{-}1,\, m{+}t{-}1\rangle.\end{aligned} \tag{A.2}$$

It can further be shown that a pair of first-order terms $jklm$ and $pqrt$ will contribute to the second order term $h^{(2)}_{abcd}$ precisely when the Poisson bracket $\{|jklm\rangle\,,\,|pqrt\rangle\}$ produces a ket $|abcd\rangle$ in the right-hand side of Eq. (A.2) [4, 9]. This formulation is equivalent to the selection rules in Eq. (3.13). The coefficients 18 and 6 in Eq. (3.14) stem from the factor $2i(jq-kp)$ in Eq. (A.2) as illustrated by

$$\begin{aligned}\{\,|3000\rangle\,,\,|0300\rangle\,\} &= 18i\,|2200\rangle\,, \\ \{\,|2100\rangle\,,\,|1200\rangle\,\} &= 6i\,|2200\rangle\,.\end{aligned} \tag{A.3}$$

Following the exact same procedure, the second-order correction of the coupled detuning term h_{1111} is given by [4,9]

$$\begin{aligned} h^{(2)}_{1111} = \;& \mathrm{Im}\Big[4\,f^{(1)}_{0111}\,h^{(1)}_{2100} + 4\,f^{(1)}_{1200}\,h^{(1)}_{1011} + 8\,f^{(1)}_{0102}\,h^{(1)}_{1020} - 8\,f^{(1)}_{0120}\,h^{(1)}_{1002}\Big] \\ & - \int_0^C \mathrm{d}s\,\mathrm{Im}\Big[4\,G_{0111}(s)\,h^{(1)}_{2100}(s) + 4\,G_{1200}(s)\,h^{(1)}_{1011}(s) \\ & \qquad + 8\,G_{0102}(s)\,h^{(1)}_{1020}(s) - 8\,G_{0120}(s)\,h^{(1)}_{1002}(s)\Big], \end{aligned} \tag{A.4}$$

and the correction for the vertical detuning h_{0022} by

$$\begin{aligned} h^{(2)}_{0022} = \;& \mathrm{Im}\Big[2\,f^{(1)}_{0111}\,h^{(1)}_{1011} + 2\,f^{(1)}_{0120}\,h^{(1)}_{1002} + 2\,f^{(1)}_{0102}\,h^{(1)}_{1020}\Big] \\ & - \int_0^C \mathrm{d}s\,\mathrm{Im}\Big[2\,G_{0111}(s)\,h^{(1)}_{1011}(s) + 2\,G_{0120}(s)\,h^{(1)}_{1002}(s) \\ & \qquad + 2\,G_{0102}(s)\,h^{(1)}_{1020}(s)\Big]. \end{aligned} \tag{A.5}$$

As with α, the TRIBs parameters α_{xy} and α_{yy} can be expressed in the calculation-friendly form derived in Section 3.2.4, which is included for completeness. Applying this framework to Eqs. (A.4), (A.5) and (3.23) yields

$$
\begin{aligned}
\alpha_{xy} &= \sum_{u,v} k_2^{(u)} \mathcal{G}_{\alpha_{xy}}^{(uv)} k_2^{(v)} + \sum_{u} k_3^{(u)} \mathcal{G}_{\alpha_{xy}}^{(u)}, \\
\alpha_{yy} &= \sum_{u,v} k_2^{(u)} \mathcal{G}_{\alpha_{yy}}^{(uv)} k_2^{(v)} + \sum_{u} k_3^{(u)} \mathcal{G}_{\alpha_{yy}}^{(u)},
\end{aligned}
\tag{A.6}
$$

where the coefficients in Eq. (A.6) are given by

$$
\begin{aligned}
\mathcal{G}_{\alpha_{xy}}^{(uv)} &= -\frac{2}{\pi} \mathrm{Im} \left[4\mathcal{G}_{\substack{2100\\0111}}^{AB\,(uv)} + 4\mathcal{G}_{\substack{1011\\1200}}^{AB\,(uv)} + 8\mathcal{G}_{\substack{1020\\0102}}^{AB\,(uv)} - 8\mathcal{G}_{\substack{1002\\0120}}^{AB\,(uv)} \right], \\
\mathcal{G}_{\alpha_{xy}}^{(u)} &= -\frac{2}{\pi} \mathcal{G}_{1111}^{(u)}, \\
\mathcal{G}_{\alpha_{xy}}^{(uv)} &= -\frac{4}{\pi} \mathrm{Im} \left[2\mathcal{G}_{\substack{1011\\0111}}^{AB\,(uv)} + 2\mathcal{G}_{\substack{1002\\0120}}^{AB\,(uv)} + 2\mathcal{G}_{\substack{1020\\0102}}^{AB\,(uv)} \right], \\
\mathcal{G}_{\alpha_{yy}}^{(u)} &= -\frac{4}{\pi} \mathcal{G}_{0022}^{(u)}.
\end{aligned}
\tag{A.7}
$$

Here, the coefficients $\mathcal{G}^{A\,(uv)}$ and $\mathcal{G}^{B\,(uv)}$ have been combined according to

$$
\mathcal{G}_{\substack{jklm\\pqrt}}^{AB\,(uv)} = \mathcal{G}_{\substack{jklm\\pqrt}}^{B\,(uv)} - \mathcal{G}_{\substack{jklm\\pqrt}}^{A\,(uv)}
\tag{A.8}
$$

for compactness.

Appendix B: Calibration of Optical Magnification

The magnification of an imaging system can be measured by shifting the lens (and therefore the optical axis) transversely while measuring the movement of the image of a stationary object on the CCD sensor, as illustrated in Fig. B.1. From this diagram, the following relations hold

$$\begin{aligned} b &= -Ma, & \Delta &= a - a', \\ b' &= -Ma', & \Delta_I &= b - b' + \Delta, \end{aligned} \tag{B.1}$$

where M is the lens magnification and Δ_I is the signed distance of the image shift. From Eq. (B.1) it follows that

$$\Delta_I = -(M+1)\Delta. \tag{B.2}$$

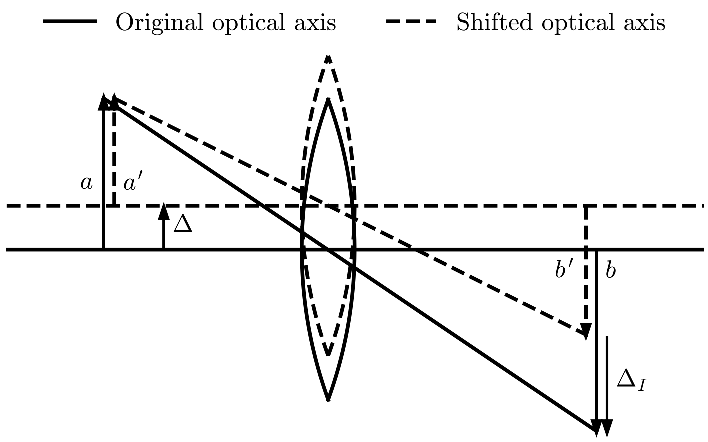

Figure B.1: An optical diagram illustrating how the image (right-hand side) of a stationary object (left-hand side) moves when the optical axis is shifted a distance Δ by moving the lens. The arrows denote the signed distances from the optical axis.

Table B.1: The measured magnifications for both diagnostic beamlines.

Beamline	Measured magnification	Uncertainty (1σ)
A	1.6340	0.0015
B	1.2466	0.0017

It is possible to use this measurement technique in the diagnostic beamlines as the lenses are mounted on linear stages. The beam itself is used as the stationary object, and Δ_I is measured using a gaussian fit of the beam profile, taking the CCD pixel size into account. The magnification is then given by a linear fit of Δ_S as a function of Δ. Such a measurement is exemplified in Fig. B.2, and the results detailed in Tab. B.1. While the residuals show some remaining structure possibly caused by non-linear aberrations, the amplitudes of the residuals are low enough that the optics of both beamlines are deemed to be linear.

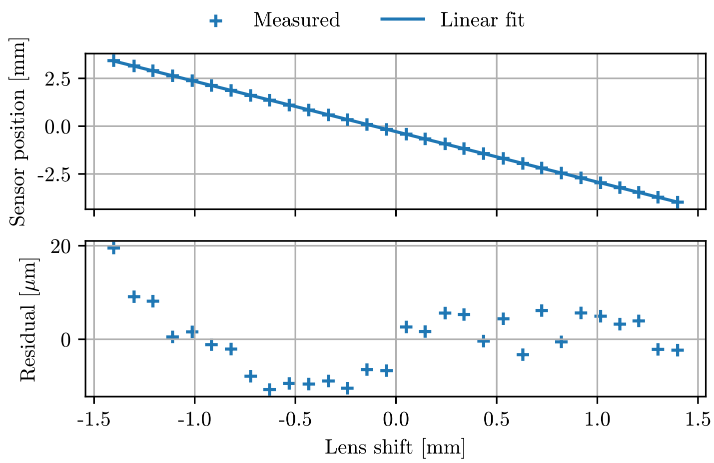

Figure B.2: An example showing the results of a magnification measurement on diagnostic beamline A.

Appendix C: Detailed Tune Scan Implementation

The tune scan technique detailed in Section 5.2.1, requires measuring the islands orbits at a range of different horizontal core tunes. The procedure repeated for each tune is detailed below for completeness.

1. The beam is driven to the core. A transverse excitation is applied so that the tune spectra can be measured.

2. The tune feedback system is enabled to correct the tunes to the setpoints for Q_x and Q_y. At the same time, the orbit feedback systems in both planes are enabled to correct the orbit. Once the tunes have stabilized, all feedback systems are disabled.

3. A set of $n = 50$ tune spectra are recorded at a frequency of 5 Hz, after which the transverse excitations are disabled.

4. The core position is measured using images from both diagnostic beamlines as well as the BPMs. These measurements are repeated $n = 10$ times at a frequency of 1 Hz.

5. Once all of the data from the core orbit has been collected, the beam is driven to the island orbits.

6. The island orbits are measured using the diagnostic beamlines and BPMs in an identical manner to step 4.

7. The transverse excitations are enabled, and the island tunes are measured as in step 3. The excitations are then disabled.

Before the scan, a machine configuration file is saved to be used as a basis for the LOCO fit, and the chromaticity is measured.

It was noted that after the tune feedback was disabled, the island and core tunes would drift noticeably over relatively fast timescales of just tens of seconds. This unfortunately meant that the condition had time to change between the core and island measurements, which could not be later accounted for in the data analysis.